INVESTIGATION OF TRACER GAS VARIABILITY FROM OBSERVATIONS AND MODELS

A Dissertation Presented to
the Faculty of the Department of Earth and Atmospheric Sciences
University of Houston

In Partial Fulfillment
of the Requirements for the Degree
Doctor of Philosophy

By

Jingqian Wang

May 2012

INVESTIGATION OF TRACER GAS VARIABILITY FROM OBSERVATIONS AND MODELS

_____

Jingqian Wang

APPROVED:

_____

Dr. Xun Jiang, Chairman

_____

Dr. Bernhard Rappenglueck

_____

Dr. Barry Lefer

_____

Dr. Yuk Yung, California Institute of Technology

_____

Dean, College of Natural Sciences and Mathematics

ACKNOWLEDGEMENTS

My deepest gratitude goes to my advisor, Dr. Xun Jiang. Without her guidance, support, and encouragement, I would not have been able to finish this dissertation in a timely manner. She has showed me what a true scientist is, and her boundless enthusiasm for research has inspired me throughout my graduate career.

I would like to thank my committee members, Dr. Bernhard Rappenglueck, Dr. Barry Lefer, and Dr. Yuk Yung for their valuable comments and advice in finalizing this research. I would also like to acknowledge my colleagues, Baijun Tian, Edward T. Olsen, Liming Li, Luke L. Chen, Maochang Liang, Run-Lie Shia, Stephen Licata, Steven Pawson, and Thomas Pagano.

I would also like to thank Scribendi for editing my dissertation.

Finally, my special appreciation goes to my family, to my parents, parents-in-law, and my husband, Heng Li. Without their support and sacrifice, this dissertation would not have been possible.

INVESTIGATION OF TRACER GAS VARIABILITY FROM OBSERVATIONS AND MODELS

An Abstract of a Dissertation
Presented to
the Faculty of the Department of Earth and Atmospheric Sciences
University of Houston

In Partial Fulfillment
of the Requirements for the Degree
Doctor of Philosophy

By

Jingqian Wang

May 2012

Abstract

The variability of the tracer gases CO_2 and ozone was investigated utilizing *in-situ* measurements, satellite retrievals, and model simulations.

In the tropical region, using Atmospheric Infrared Sounder (AIRS) mid-tropospheric CO_2 retrievals led to the discovery of a signal with a periodicity of around two years, which was found to be related to the Tropospheric Biennial Oscillation (TBO). During strong (weak) monsoon years, the Western Walker Circulation was strong (weak), resulting in more (less) CO_2 in the mid-troposphere. The MOZART-2 model results were consistent with observations with a smaller amplitude.

In the North Hemisphere polar region, the influence of sudden stratospheric warming (SSW) on AIRS CO_2 was investigated. The Eliassen-Palm flux divergence was negative before the SSW; as a result, the westerly wind in the stratosphere decreased. During the SSW, the polar zonal mean wind switched to easterly and the temperature increased. Mid-latitude CO_2 was transported to the high latitudes, leading to an increase of mid-tropospheric CO_2 concentrations in the polar region.

Over the Central Pacific Ocean, the influence of El Niño on the mid-tropospheric CO_2 was investigated using the MOZART-2 model. Model simulation results were consistent with the observations. There was more (less) mid-tropospheric model CO_2 in the central Pacific and less (more) mid-tropospheric model CO_2 in the western Pacific during El Niño (La Niña) events.

In addition to exploring these CO_2 variations, the impacts of ENSO on the tropical total column ozone, the tropical tropopause pressure, and the 3.5-yr ozone signal in the mid-latitude were also investigated. Both the observations and Goddard Earth Observing System Chemistry-Climate Model (GEOS CCM) show tropical tropopause pressure to be related to the ENSO signal in the total column ozone. The GEOS CCM was also used to investigate a possible mechanism for the 3.5-yr signal observed in the mid-latitude total column ozone. Results suggested that a model with realistic ENSO could reproduce the 3.5-yr signal. Hence, it is likely that the 3.5-yr signal was caused by ENSO.

Table of Contents

List of Figures

PAGE

List of Tables

Chapter 1

Introduction

Broadly, this dissertation aims to investigate the variability of the tracer gases carbon dioxide and ozone using satellite and observations and simulation models.

The trend and annual cycles of carbon dioxide have been well studied over the past several decades (Pearman and Hyson, 1980, 1981; Cleveland *et al.*, 1983; Bacastow *et al.*, 1985; Keeling *et al.*, 1995; Keeling *et al.*, 1996; Buermann *et al.*, 2007). Surface observations show that CO_2 level keeps increasing with a trend of ~ 2 ppm/yr, primarily as a result of increases in fossil fuel emission (Keeling *et al.,* 1995). The natural sources of atmospheric CO_2 include volcanic outgassing, the combustion of organic matter, and the respiration processes of living aerobic organisms. The anthropogenic sources are mainly fossil fuel combustion, biomass burnings, and deforestation. Most of these sources are near the surface. The uptake and release of CO_2 by vegetation also plays a very important role in the CO_2 annual cycle amplitude, which is larger in the northern hemisphere (NH) than in the southern hemisphere (SH).

In addition to the surface CO_2 emissions, atmospheric transport processes also influence the mixing ratio and distribution of the atmospheric CO_2 (Jiang *et al.*, 2010; Li *et al.*, 2010). Recent global satellite CO_2 retrievals provide a unique opportunity to explore the CO_2 variations originating from the transport processes and surface CO_2

emissions. In this dissertation, I combine the satellite retrievals with *in-situ* measurements and model simulations to explore the CO_2 variations.

Ozone, another important trace gas, is known as protector of life on Earth from the sun's ultraviolet radiation. The French physicists Charles Fabry and Henri Buisson first discovered the ozone layer in 1913. It is in the lower portion of the stratosphere, from approximately 30 to 40 kilometers above Earth, and with a thickness that varies seasonally and geographically. The British meteorologist G. M. B. Dobson (1931) developed a spectrophotometer (the Dobson meter) and used it to measure stratospheric ozone from the ground. Between 1928 and 1958, a worldwide network of ozone monitoring stations was established, which continues to operate today.

One of the most common ozone measurements is that of total amount. Other measurements include partial pressure, number density, and concentration at particular altitudes. Total column ozone demonstrates the inter-annual variability due to the influence of the large-scale circulations (Bojkov, 1987; Zerefos *et al.,* 1992; Kayano, 1997). It has been found that Quasi-Biennial Oscillation, El Niño, and volcanic eruption can modulate the total column ozone concentration (Bojkov, 1987). The occurrence of El Niño events, for example, are followed a few months later by a decrease in total column ozone (Bojkov, 1987), with the delay in the middle to high latitudes being longer than that in the tropics. I explore the influence of El Niño on total column ozone using a chemistry-climate model in this dissertation.

1.1 Motivation

It has long been known that the increasing level of atmospheric CO_2 is significantly affecting the global climate (Dickinson and Cicerone, 1986). The increase in CO_2 concentrations is primarily a result of the increase in fossil fuel emission (Keeling *et al.,* 1995). In addition to the trend and annual cycle of CO_2, atmospheric CO_2 also demonstrates interesting intraseasonal and interannual variability. Li *et al.* (2010) found that CO_2 anomalies in the mid-troposphere could propagate to the east as a response to an intraseasonal variation named the 'Madden-Julian Oscillation' (MJO). The amplitude of the MJO signal in mid-tropospheric CO_2 is about 1 ppm (Li *et al.*, 2010).

El Niño and the Southern Oscillation (ENSO), an important large-scale, inter-annual climate variability in the tropical region, can also influence CO_2 concentrations. Atmospheric CO_2 is influenced by the ENSO at the surface (Bacastow, 1976; Bacastow *et al.*, 1980). During El Niño events, the atmospheric CO_2 growth rates increase at surface stations (Keeling *et al.*, 1995; Jones *et al.*, 2001; Nevison *et al.*, 2008), while during La Niña events, the atmospheric CO_2 growth rates decrease at the surface stations. Using mid-tropospheric CO_2 satellite data, Jiang *et al.* (2010) found that ENSO could also influence the mid-tropospheric CO_2 concentration. Mid-tropospheric CO_2 is enhanced in the central Pacific Ocean and diminished in the western Pacific Ocean during El Niño (Jiang *et al.*, 2010).

In this study, I investigate the variability of CO_2 using *in-situ* CO_2 measurements (surface and aircraft), CO_2 retrievals from the Atmospheric Infrared Sounder (AIRS) satellite instrument, and three-dimensional (3-D) chemistry-transport models.

Specifically, I explored the influences of ENSO and Tropospheric Biennial Oscillation (TBO) on CO_2, and use satellite CO_2 retrieval to better understand the influence of the large-scale dynamics on the tracer gas in the North Hemisphere (NH) polar region.

Understanding precisely how ozone abundances will change in the future with diminished chlorofluorocarbon emissions remains an important challenge for atmospheric scientists. To better understand the long-term trend in ozone, I need also to understand its interannual variability as a result of large-scale circulation. In this dissertation, I use a chemistry-climate model (GEOS-CCM) to simulate and explore the influence of ENSO on the total column ozone in the tropics and mid-latitude.

1.2 Dissertation Overview

This dissertation focuses on studying the variability of carbon dioxide and ozone using satellite and also observations and simulation models.

In Chapter 2, I first use mid-tropospheric CO_2 retrievals from the Atmospheric Infrared Sounder (AIRS) to study the global trend and annual cycle of CO_2. Then I explore the CO_2 interannual variability over the Indo-Pacific region. A signal with periodicity around two years is discovered for the AIRS mid-tropospheric CO_2 over the Indo-Pacific region. This is related to the TBO associated with the strength of the monsoon. During a strong (weak) monsoon year, the Western Walker Circulation is strong (weak), resulting in enhanced (diminished) CO_2 transport from the surface to the mid-troposphere. As a result, there are positive (negative) CO_2 anomalies at mid-troposphere over the Indo-Pacific region during strong (weak) monsoon years. I also

simulate the influence of the TBO on mid-tropospheric CO_2 over the Indo-Pacific region using the Model of Ozone and Related Chemical Tracers version 2 (MOZART-2). Results from MOZART-2 are consistent with observations, although the TBO signal in the model CO_2 is smaller than that in the AIRS mid-tropospheric CO_2.

In Chapter 3, I use AIRS mid-tropospheric CO_2 to explore the influence of sudden stratospheric warming (SSW) on CO_2 in the NH polar region. Observation results demonstrate that the polar mid-tropospheric CO_2 increase during major stratospheric warming. To better investigate the influence of SSW on tracers, I also calculate the Eliassen-Palm (EP) flux and divergence. The EP-flux divergence is negative before the SSW, and the westerly wind in the stratosphere decreases. During the SSW, the polar zonal mean wind switches to easterly and the temperature increases by about 4 K. The polar vortex is much weaker during the SSW. Mid-latitude CO_2 is transported to high latitudes and leads to an increase in mid-tropospheric CO_2 concentrations in the polar region, which is seen in the AIRS CO_2 retrievals.

In Chapter 4, I investigate the influence of El Niño on the AIRS mid-tropospheric CO_2 retrievals and MOZART-2 model. AIRS mid-tropospheric CO_2 data are used to investigate the temporal and spatial variability of CO_2 as a response to El Niño. The CO_2 difference between the central and the western Pacific correlates well with the Southern Oscillation Index. A multiple regression method is also utilized to investigate the El Niño signal in the AIRS mid-tropospheric CO_2 from September 2002 to February 2011. There is more (less) mid-tropospheric CO_2 in the central Pacific and less (more) mid-

tropospheric CO_2 in the western Pacific during El Niño (La Niña) events. Similar results are seen in the MOZART-2 mid-tropospheric CO_2, although the ENSO signal in the model is weaker than that in the AIRS mid-tropospheric CO_2.

In Chapter 5, I examine the impacts of El Niño-Southern Oscillation (ENSO) on the tropical total column ozone, the tropical tropopause pressure, and the 3.5-yr ozone signal in the mid-latitude total column ozone using the Goddard Earth Observing System Chemistry-Climate Model (GEOS CCM). Observed monthly mean sea surface temperature and sea ice between 1951 and 2004 are used as boundary conditions for the model. Since the model includes no solar cycle, quasi-biennial oscillation, or volcanic forcing, the ENSO signal is found to dominate the tropical total column ozone variability. A principal component analysis is applied to the detrended, deseasonalized, and low-pass filtered model outputs. The first mode of model total column ozone captures 63.8% of the total variance. The spatial pattern of this mode is similar to that in Total Ozone Mapping Spectrometer (TOMS) observations. There is also a clear ENSO signal in the tropical tropopause pressure in the GEOS CCM, which is related to the ENSO signal in the total column ozone. The regression coefficient between the model total column ozone and the model tropopause pressure is 0.71 Dobson units (DU)/hPa. The GEOS CCM is also used to investigate a possible mechanism for the 3.5-yr signal observed in the mid-latitude total column ozone. The 3.5-yr signal in the GEOS CCM column ozone is similar to that in the observations, which suggests that a model with realistic ENSO can reproduce the 3.5-yr signal. Hence, it is likely that the 3.5-yr signal is caused by ENSO.

Chapter 2

The Influence of Tropospheric Biennial Oscillation on Mid-tropospheric CO_2

2.1 Introduction

Carbon dioxide is the most important anthropogenic greenhouse gas in the atmosphere and its continued increase is of serious concern, since it can have an adverse climatic impact (see, e.g., IPCC, 2007). Current satellite missions provide global measurements of atmospheric CO_2, which can be used to characterize CO_2 sources and sinks on regional scales and transport of CO_2 around the globe (Yokota *et al.*, 2009; Boesch *et al.*, 2011). It is important to identify and quantify spatiotemporal patterns of the natural variability of CO_2 before carrying out inversions for net CO_2 sources and sinks associated with anthropogenic activities. Recent studies have identified CO_2 natural variability arising from El Niño (Jiang *et al.*, 2010), Madden Julian Oscillation (Li *et al.,* 2010), and synoptic weather in the mid-latitudes (Keppel-Aleks *et al.*, 2011).

A previous study (Li *et al.*, 2005) revealed that more CO could appear in the upper troposphere over the Tibetan Plateau and Southwest China during the Asian summer monsoon seasons. In this chapter, I focus on investigating the influence of TBO on the Atmospheric Infrared Sounder (AIRS) CO_2 data in the mid-troposphere. I first introduce

data and model in Sections 2.2 and 2.3. Then, I explore the trend, seasonal cycle, and standard deviations of the AIRS mid-tropospheric CO_2 in Section 2.4. Finally, I investigate the influence of TBO on the AIRS mid-tropospheric CO_2 in Section 2.5.

2.2 Data

The CO_2 data employed in this dissertation are retrieved from AIRS (Chahine *et al.,* 2005; Chahine *et al.,* 2008). AIRS is an instrument on NASA's Aqua satellite, which has been orbiting earth in a sun-synchronous near-polar orbit since 2002. It is a cross-track scanning grating spectrometer with 2378 channels from 3.7 to 15.4 μm with a 13.5 km field of view at nadir (Aumann *et al.,* 2003). The channel with a range of 690–725 cm^{-1} is selected to retrieve mid-tropospheric CO_2. It is the first time we have been able to retrieve data on daily CO_2 concentrations globally, over land and ocean, day and night, even in the presence of clouds. The mixing ratios of mid-tropospheric CO_2 are retrieved using the Vanish Partial Derivative Method (VPD) (Chahine *et al.,* 2005; Chahine *et al.,* 2008).

The maximum sensitivity of AIRS mid-tropospheric CO_2 is between 500 hPa and 300 hPa. AIRS Version 5 CO_2 retrievals are available at 2º× 2.5º (latitude by longitude) from September 2002 to February 2010. Olsen *et al.* (2011) found that the AIRS CO_2 accuracy is within 2 ppm under clear and cloudy conditions and over both land and oceans between 30°S and 80°N, after comparing AIRS mid-tropospheric CO_2 with in-situ aircraft measurements and retrievals of measurements by land-based upward looking Fourier Transform Interferometers (Washenfelder *et al.,* 2006).

In this chapter, I use the mid-tropospheric CO_2 AIRS retrievals to investigate variability of mid-tropospheric CO_2, especially the influence of the TBO on the mid-tropospheric CO_2. Mixing ratios of AIRS mid-tropospheric CO_2 are retrieved by the Vanishing Partial Derivative Method (Chahine *et al.*, 2005; Chahine *et al.*, 2008). The maximum sensitivity of AIRS mid-tropospheric CO_2 retrievals is between 500 hPa and 300 hPa. AIRS Version 5 CO_2 retrieval products are available from 60°S to 90°N over land and ocean, day and night from the Goddard Earth Sciences Data and Information Services Center, and cover the period from September 2002, ongoing. I regridded AIRS Level 2 Standard Product CO_2 from 2º× 2.5º to 2º× 10º (latitude by longitude).

Tropical Rainfall Measuring Mission (TRMM) and Global Precipitation Climatology Project (GPCP V 2.1) precipitation data are also used to construct the Indian monsoon rainfall index. TRMM precipitation data are available at 0.25º× 0.25º (latitude by longitude) from 50ºS to 50ºN from 1998 to 2010. TRMM calibrated precipitation data combine precipitation estimates from different instruments (TMI, AMSR-E, SSM/I, AMSU-B) (Huffman *et al.*, 2007). GPCP Version 2.1 precipitation data are obtained by merging infrared and microwave satellite estimates of precipitation with rain gauge data from more than 6,000 stations (Huffman *et al.*, 2009). GPCP global monthly mean precipitation data are from 1979 to 2009 with spatial resolution 2.5°× 2.5° (latitude by longitude). Precipitation data in the monsoon season (June to September, JJAS) are used to calculate the Indian monsoon rainfall index (area mean of JJAS rainfall in 5°N~40°N, 60°E~100°E), which determines monsoon strengths in different years (Meehl and Arblaster, 2002). A relatively strong monsoon is defined as on in which precipitation (P_i)

is higher than the two adjacent years ($P_{i-1} < P_i > P_{i+1}$), with a relatively weak monsoon one in which the precipitation is lower ($P_{i-1} > P_i < P_{i+1}$).

2.3 Model

I use a three-dimensional (3-D) chemistry-transport model, the second (most recent) version of the Model of Ozone and Related Chemical Tracers (MOZART-2), to investigate the TBO signal in mid-tropospheric CO_2. ECMWF-Interim meteorological data are used to drive MOZART-2. The horizontal resolution is 2.8° (latitude) × 2.8° (longitude) and there are 45 vertical levels extending up to an altitude of approximately 50 km (Horowitz *et al.,* 2003). MOZART-2 is built on the framework of the Model of Atmospheric Transport and Chemistry (MATCH). MATCH includes representations of advection, convective transport, boundary layer mixing, and wet and dry deposition. The surface boundary condition for MOZART-2 is the prescribed CO_2 source/sink flux boundary condition, as described in Jiang *et al.* (2008a). The exchange of CO_2 between the terrestrial biosphere and atmosphere is based on net primary productivity and respiration fluxes from the Carnegie-Ames-Stanford (CASA) ecosystem model (Randerson *et al.*, 1997). Air-to-sea exchange of CO_2 is from Takahashi *et al.* (1997). Estimates of fossil fuel emissions are from Marland *et al.* (2007). Monthly mean biomass burning emissions of CO_2 are derived based on Duncan *et al.* (2003). I use the climatological CO_2 surface fluxes in this study. There is no interannual variation in the CO_2 surface flux boundary condition for the MOZART-2 model.

2.4 Trend, Seasonal Cycle, and Standard Deviations of AIRS Mid-tropospheric CO_2

In order to understand the trend of CO_2 in the mid-troposphere, I first calculate the AIRS mean mid-tropospheric CO_2 averaged from 60ºS to 90ºN. A time series for the mean AIRS mid-tropospheric CO_2 is shown in Figure 2.1. The trend of AIRS mean mid-tropospheric CO_2 is about 2 ppm/year from 2003 to 2009, which is related to the positive trend in the surface CO_2 due to increased fossil fuel emission (Keeling *et al.,* 1995).

The concentrations of atmospheric CO_2 are closely related to season and terrestrial vegetation. When vegetation grows, it removes CO_2 from the atmosphere. Usually, the plants start to grow in May in the Northern Hemisphere (NH) and absorb carbon dioxide by photosynthesis, so the concentrations of CO_2 begin to decrease after May. In the autumn, most vegetation dies and decays. Leaves will fall from deciduous trees and give off carbon dioxide during decomposition. As a result, the atmospheric carbon dioxide levels rise from the fall in the middle and high latitudes. This removing and returning creates the seasonal cycle in the atmosphere's CO_2 concentrations.

In order to reveal the seasonal cycle of mid-tropospheric CO_2, I plot the AIRS mid-tropospheric CO_2 in January, April, July, and October in Figure 2.2. In the NH, AIRS mid-tropospheric CO_2 concentrations are low in January, which is related to the redistribution of stratospheric low concentrations of CO_2 into the mid-troposphere (Chahine *et al.*, 2008). AIRS mid-tropospheric CO_2 concentrations are high in April as a result of the build up of fossil fuel and biomass burnings over the winter season. Since

the plants start to grow in spring, the mid-tropospheric CO_2 concentrations decrease from April to July as a result of vegetation uptake (Figure 2.2 b and c). The mid-tropospheric CO_2 concentrations go up again in October in the NH when fall comes (Figure 2.2 d). In the Southern Hemisphere (SH), the mid-tropospheric CO_2 concentrations are high in the winter season (e.g., July) and low in the summer season (e.g., January).

To reveal variations in the AIRS mid-tropospheric CO_2, I calculate the standard deviations of the AIRS detrended mid-tropospheric CO_2 concentrations. The linear trend is removed from the AIRS mid-tropospheric CO_2 data at each grid point. The standard deviations of mid-tropospheric CO_2 are high in the middle and high latitudes in the NH, which might be related to the relatively large CO_2 seasonal cycle, intraseasonal, and interannual variations over this region. The standard deviations of mid-tropospheric CO_2 concentrations are low in the tropics, for there is more ocean than land in the tropical area. The CO_2 seasonal cycle, intraseasonal, and interannual variations are all smaller in the tropical area than those in the middle to high latitudes.

In the next section, I focus on investigating the interannual variation of the mid-tropospheric CO_2 from satellite retrievals and model simulations over the Indo-Pacific area in order to better understand the variations of CO_2 in the tropical area.

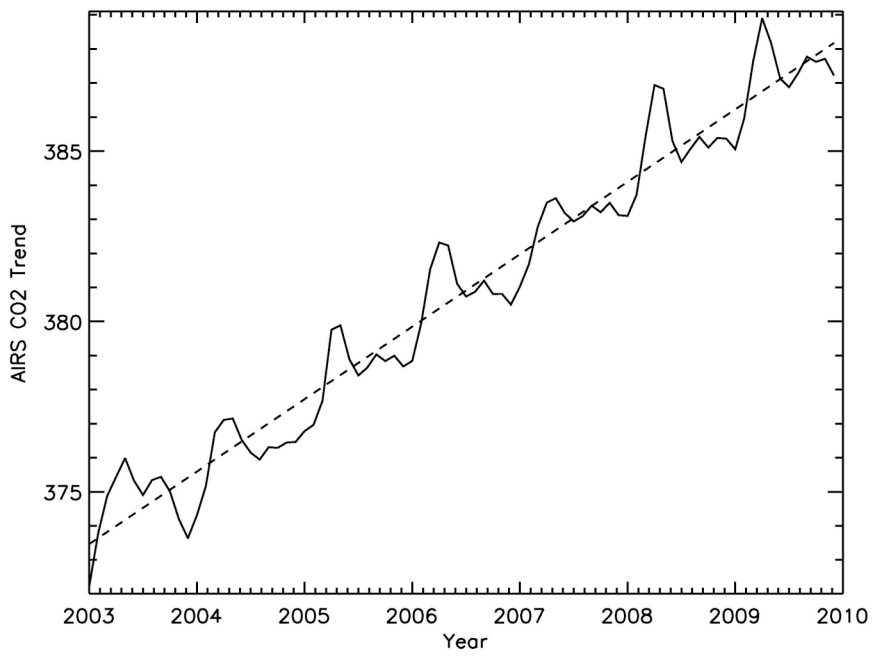

Figure 2.1. Time series of global mean AIRS mid-tropospheric CO_2 from 2003 to 2009. AIRS mid-tropospheric CO_2 were averaged over 60°S–90°N.

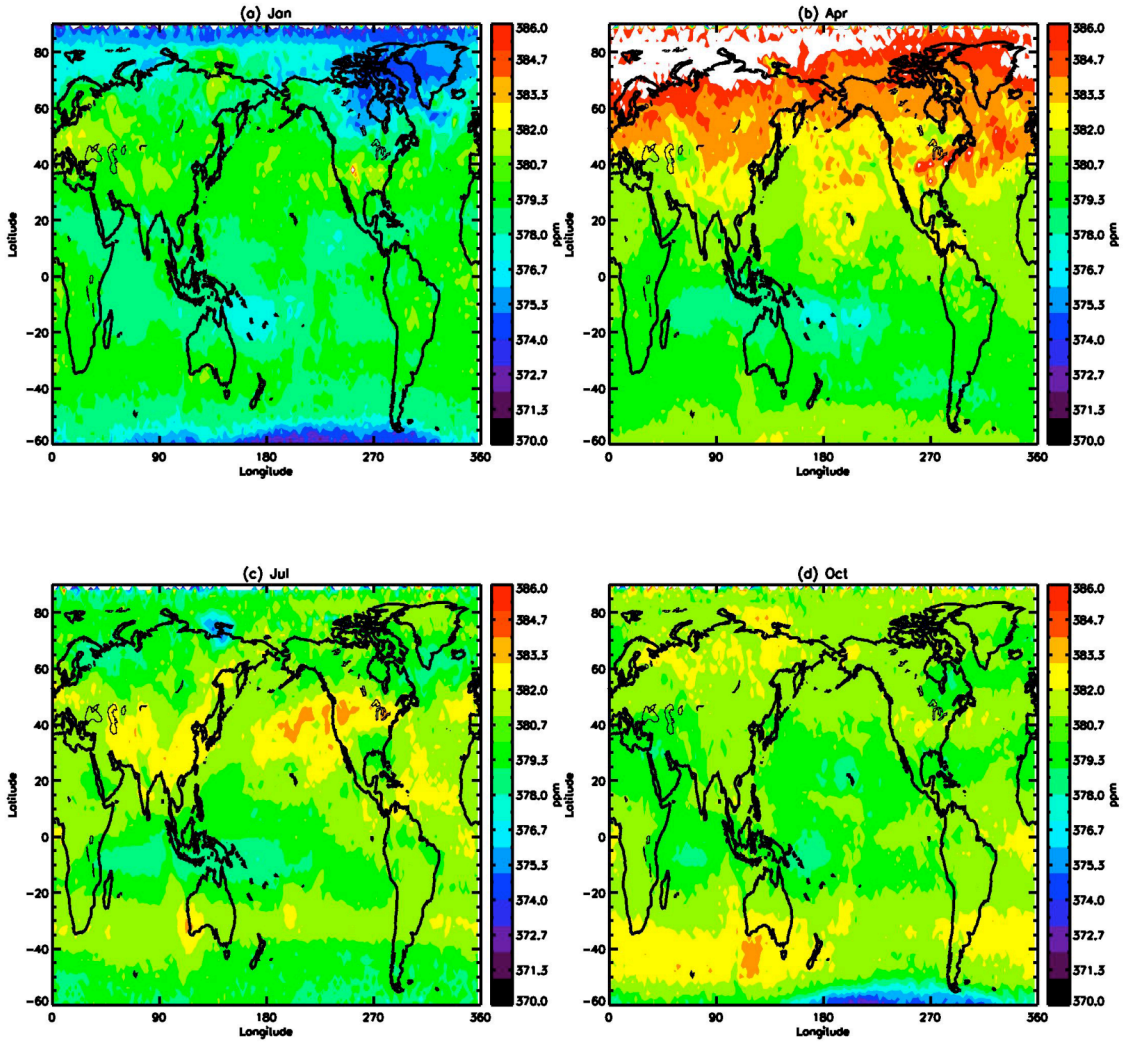

Figure 2.2. AIRS mid-tropospheric CO_2 averaged in (a) January, (b) April, (c) July, and (d) October from 2003 to 2009.

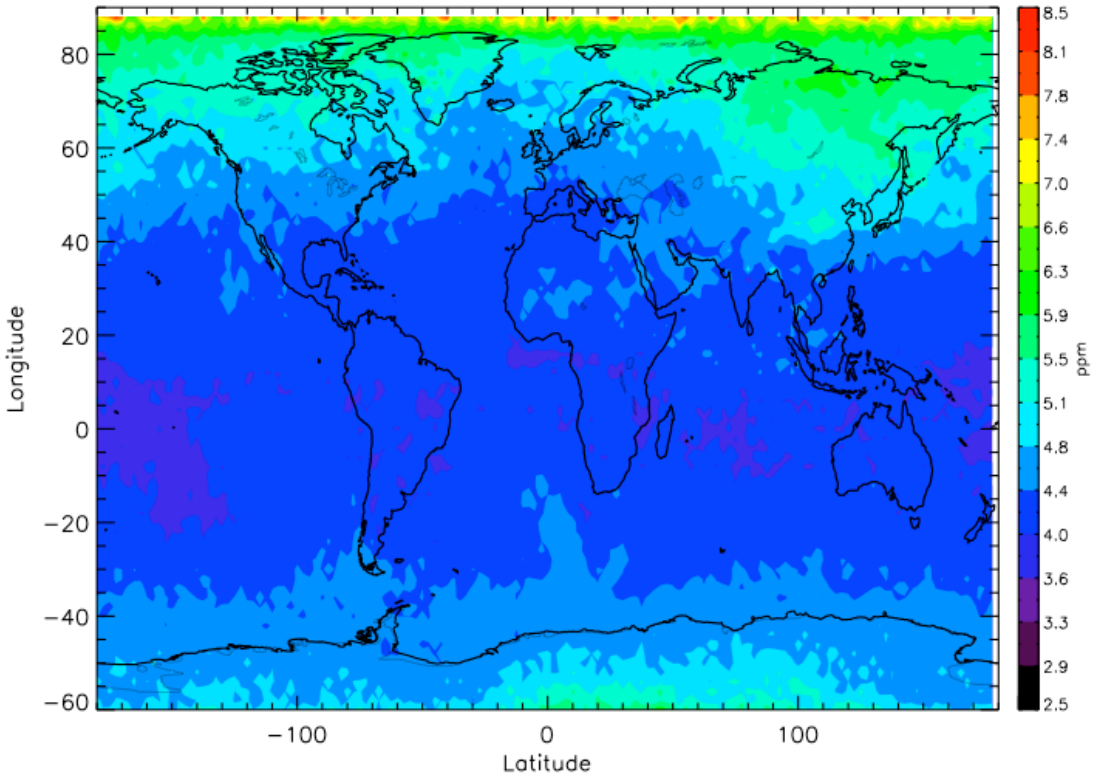

Figure 2.3. Standard deviations of AIRS detrended mid-tropospheric CO_2. Linear trend is removed from AIRS mid-tropospheric CO_2 at each grid point.

2.5 Tropospheric Biennial Oscillation Signal in CO_2

2.5.1 Relation between TBO and Monsoon

Over the Indo-Pacific region, monsoon rainfall exhibits a quasi-biennial oscillation, named the Tropospheric Biennial Oscillation (TBO) (Mooley and Parthasarathy, 1984; Yasunari and Suppiah, 1988; Yasunari, 1990, 1991; Tian and Yasunari, 1992; Shen and Lau, 1995; Webster *et al.,* 1998). One of the climate systems that influence atmospheric circulation, TBO is defined as a tendency for a relatively strong "Indo-Australian" monsoon to be followed by a relatively weak one (Mooley and Parthasarathy, 1984; Yasunari and Suppiah, 1988; Yasunari, 1990, 1991; Tian and Yasunari, 1992; Shen and

Lau, 1995; Webster *et al.*, 1999).

TBO occurs in the season prior to the monsoon and involves coupled land-atmosphere-ocean processes over a large area of the Indo-Pacific region (Meehl, 1997). Observations show that the TBO signals appear not only in the Indian-Australian rainfall records, but also in the tropospheric circulation, sea surface temperature (SST), and upper-ocean thermal fields (Yasunari, 1991; Ropelewski *et al.*, 1992; Lau and Yang, 1996; Chang and Li, 2001). TBO is an important component of the tropical ocean-atmosphere interaction system, separated from the El Niño-Southern Oscillation (Chang and Li, 2000). Following the TBO theory (Chang and Li, 2000), the warming in the western Pacific induces not only a strong monsoon, but also a stronger Western Walker Cell, and thus a surface westerly anomaly over the Indian Ocean. This westerly anomaly helps the cold sea surface temperature anomalies (SSTA) to persist through the succeeding seasons, leading to a weaker Asian monsoon and weaker Western Walker Cell in the following summer. The Western Walker Cell blows from the Indian Ocean to the western Pacific and creates a convergence area with the Eastern Walker Cell at the Indo-Pacific region (Meehl and Arblaster, 2002). The SSTA resembles those resulting from El Niño-La Niña conditions (Chang and Li, 2000). El Niño has been found to influence atmospheric CO_2 in the mid-troposphere as a result of a change in the circulation (Jiang *et al.*, 2010). TBO is expected to influence atmospheric CO_2 in the mid-troposphere as well. The way in which TBO influences the mid-tropospheric CO_2 is discussed below (Section 2.5.2).

2.5.2 Influence of TBO on AIRS Mid-tropospheric CO_2

In order to investigate the variability of the mid-tropospheric CO_2 over the Indo-Pacific region, I first calculated the deseasonalized and detrended AIRS mid-tropospheric CO_2 over 5°S–20°N, 100°E–150°E (Figure 2.4a). The seasonal cycle is removed by subtracting monthly mean CO_2 from the data, and linear trend then removed from this. The power spectrum of the deseasonalized and detrended CO_2 is shown in Figure 2.4b. In addition to the high frequency signals, there is also a signal approximately every two years in the power spectrum, which is within the 5% significance level. The two-year signal in the deseasonalized and detrended mid-tropospheric CO_2 may be related to the TBO. The statistical significance of signals in the power spectrum is obtained by comparing the amplitude of a spectral peak to the mean red noise spectrum (Gilman *et al.*, 1963; Jiang *et al.*, 2008b).

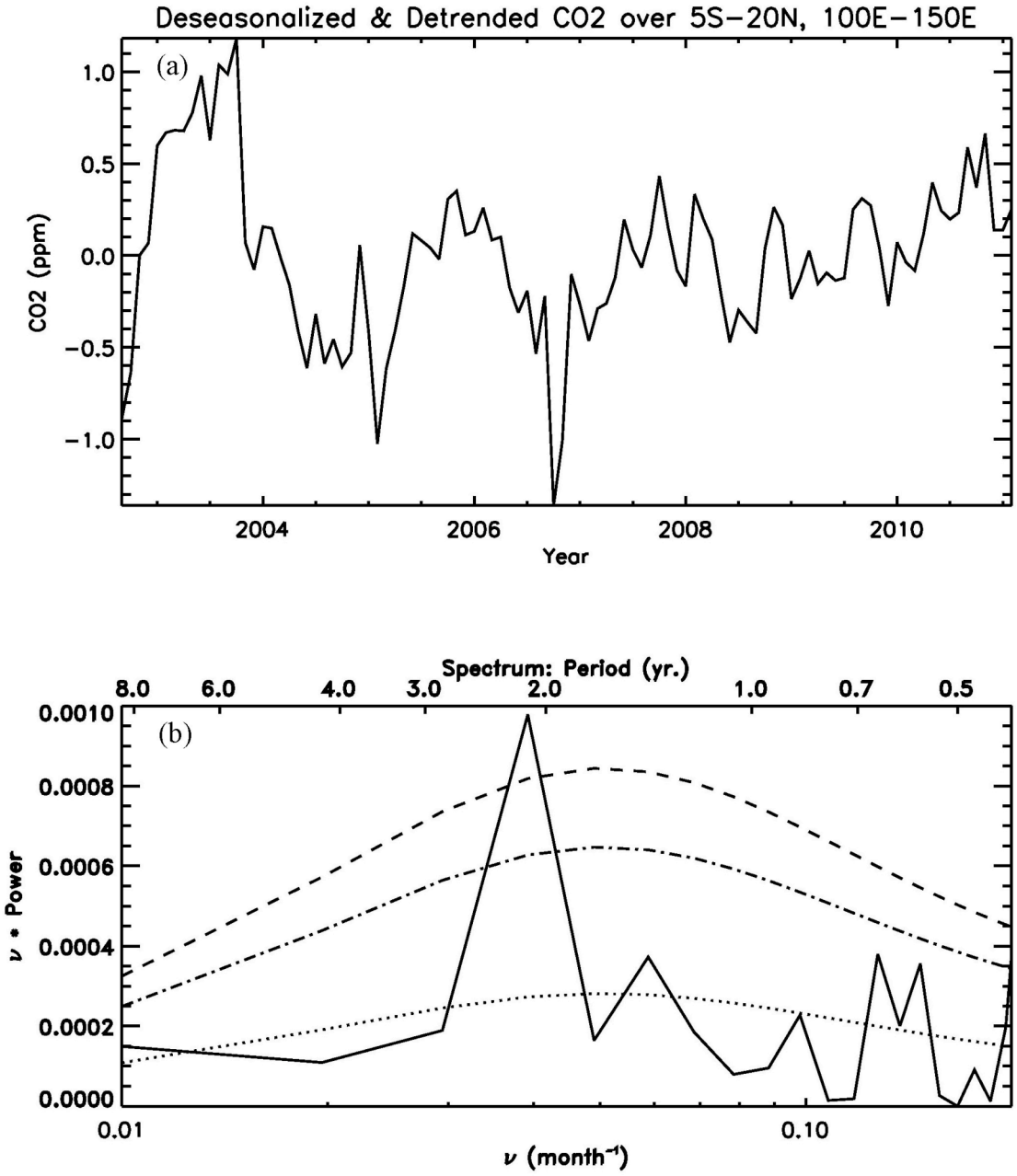

Figure 2.4. (a) Deseasonalized and detrended AIRS mid-tropospheric CO_2 averaged over 5°S–20°N, 100°E–150°E. (b) The power spectrum of deseasonalized and detrended AIRS mid-tropospheric CO_2 averaged over 5°S–20°N, 100°E–150°E. Dotted line is the mean red-noise spectrum; dash-dotted line and dashed line represent 10% and 5% significance levels, respectively.

To further investigate the possible relation between the TBO and the mid-tropospheric CO_2, I calculate AIRS detrended mid-tropospheric CO_2 during the monsoon season (JJAS), and compare it with the detrended Indian monsoon rainfall index derived from TRMM precipitation for JJAS. Results are shown in Figure 2.5. The correlation coefficient between two time series is 0.58 (4% significance level). In-phase variations show that there is more CO_2 in the mid-troposphere during the strong monsoon years (2003, 2005, 2007, and 2010), and less CO_2 during the weak monsoon years (2004, 2006, and 2008).

Li *et al.* (2010) have found that the surface CO_2 concentration was higher than the mid-tropospheric CO_2 concentration at 10–12 km (figure 2.6). They have also compared surface CO_2 at Guam (13.45°N, 144.8°E) with CONTRAIL aircraft CO_2 (10–12 km) in the summer season (JJAS) from 1994 to 2008 (Figure 2.6). The 15-year averaged CO_2 difference between the surface and aircraft in the summer season (JJAS) is 0.5 ± 0.2 ppm. This confirms that surface CO_2 concentrations are higher than that in the mid-troposphere. The transport of surface CO_2 into the mid-troposphere over the Indo-Pacific region is determined by the strength of the upwelling. From TBO (Chang and Li, 2000), the warming in the western Pacific induces not only a strong monsoon, but also a stronger Western Walker Cell. Since the Western Walker Cell is stronger during a strong monsoon year (Chang and Li, 2000), it will result in enhanced CO_2 transportation from the surface to the mid-troposphere due to the strong upwelling. Thus, there is more mid-tropspheric CO_2 over the Indo-Pacific region during a strong monsoon year. Contrarily, during a weak monsoon year, the Western Walker Cell is weaker and less CO_2 will be transported

to the mid-troposphere so less mid-tropospheric CO_2 is seen over the Indo-Pacific region. Results shown in Figure 2.5 are not contaminated by El Niño or La Niña influence, since these occur in the winter seasons (of 2005, 2008, and 2010), and thus do not overlap with Monsoon seasons (JJAS).

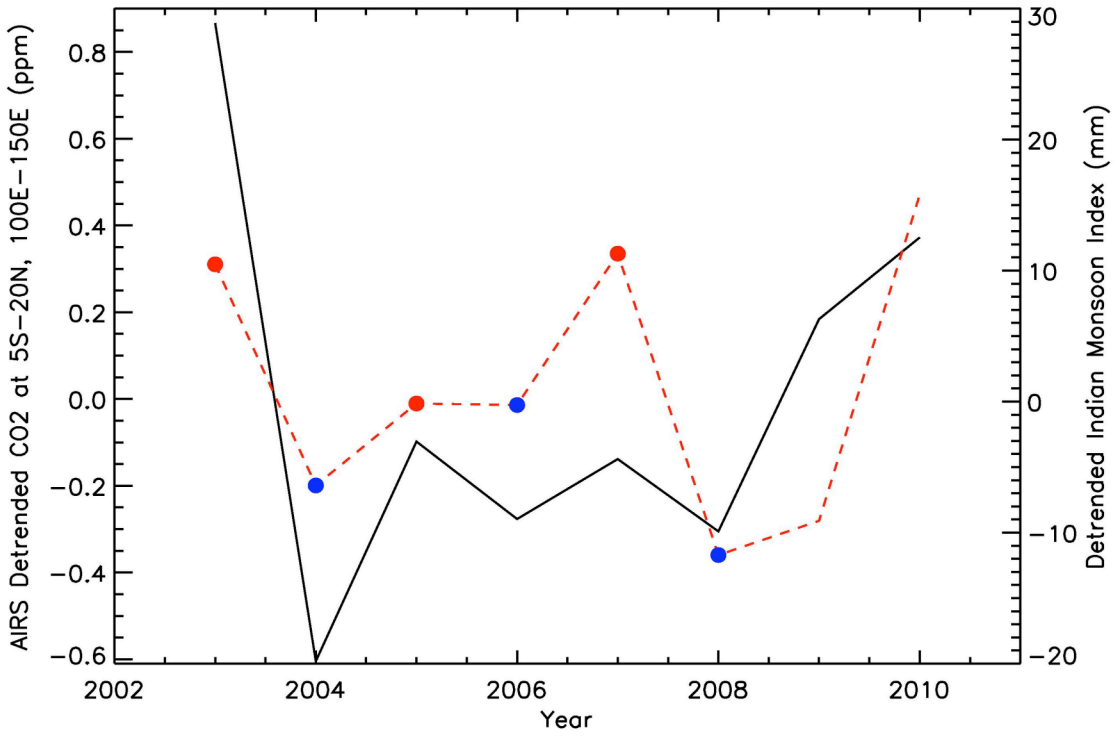

Figure 2.5. Detrended AIRS mid-tropospheric CO_2 averaged at 5°S–20°N, 100°E–150°E in JJAS from 2003 to 2010 (black solid line), and detrended Indian monsoon index calculated from TRMM precipitation data (red dashed line). Red dots are strong monsoon years, blues dots are weak monsoon years. Correlation coefficient between detrended AIRS mid-tropospheric CO_2 and detrended Indian monsoon index is 0.58 (4%).

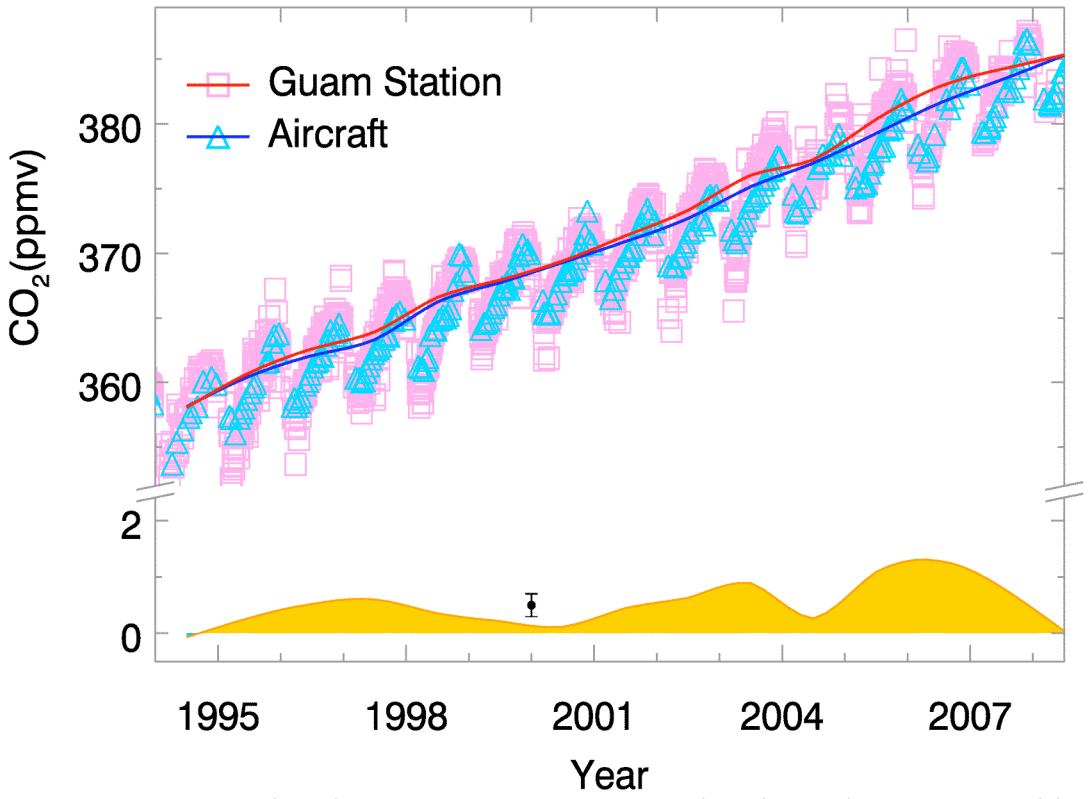

Figure 2.6. CO_2 comparison between NOAA ESRL ground station and CONTRAIL airborne flask measurements over Guam (13.45°N, 144.8°E) from June to September in each year. CONTRAIL airborne flask measurements are between 10–12 km. Each square or triangle represents an individual measurement. Red and blue lines are the CO_2 at the ground station and aircraft, respectively, averaged in the summer season (JJAS) from 1994 to 2008; yellow-filled area shows the ground CO_2 subtracted by the aircraft CO_2. The 15-yr averaged difference is 0.5 ± 0.2 ppm, plotted by the black dot and errorbar (Li *et al.,* 2010).

I investigated spatial patterns of AIRS mid-tropospheric CO_2 in both strong and weak monsoon years. The mean value of AIRS detrended mid-tropospheric CO_2 in the strong monsoon years (mean value of CO_2 in JJAS of 2003, 2005, 2007, and 2010) is shown in Figure 2.7a, and for weak monsoon years (2004, 2006, and 2008) in Figure 2.7b. In these two figures, high concentrations of the mid-tropospheric CO_2 over the Indo-Pacific region correspond to the upwelling area of the Western and Eastern Walker Cells.

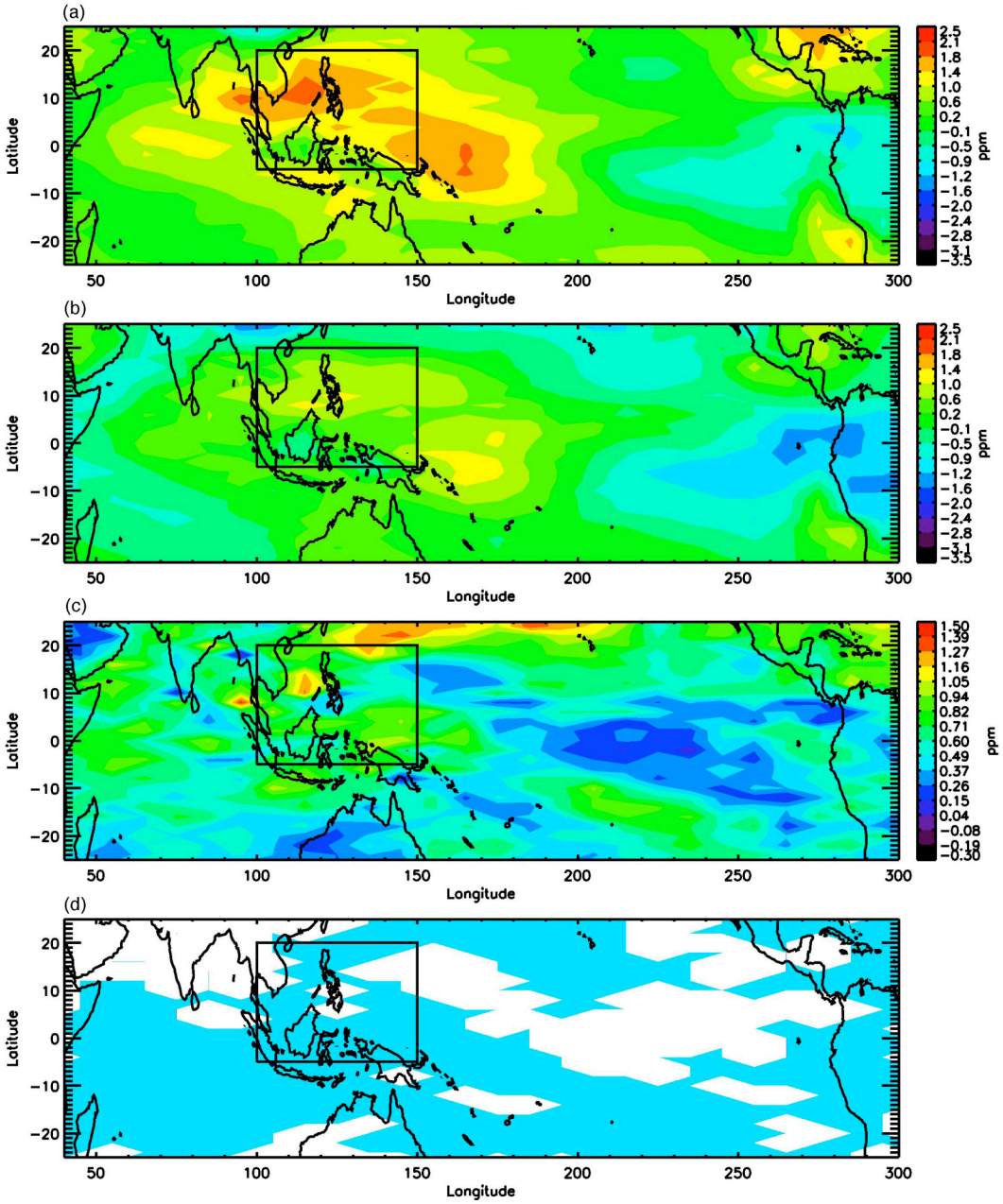

Figure 2.7. (a) Mean value of AIRS CO_2 concentration in strong monsoon years (JJAS of 2003, 2005, 2007, and 2010), (b) mean value of AIRS CO_2 concentration in weak monsoon years (JJAS of 2004, 2006, and 2008), (c) CO_2 differences between the strong and weak monsoon years, (d) CO_2 differences within 10% significance level highlighted in blue.

During strong monsoon years, there is more mid-tropospheric CO_2 over the Indo-Pacific region and the South China Sea than during weak monsoon years, though the CO_2 value over Indo-Pacific region remains high comparing the parallel latitudes outside of Indo-Pacific region (Figure 2.7c). The Student-t test is used to calculate the statistical significance of the differences for mid-tropospheric CO_2 concentrations in strong and weak monsoon years. Mid-tropospheric CO_2 differences between strong and weak monsoon years are statistically significant when the t-value is larger than a certain value t_0. There are 16 months in the strong monsoon group and 12 months in the weak monsoon group. The number of degrees of freedom for the CO_2 difference between two groups is 16+12–2 = 26. When the t-value is larger than 1.7, the results are within the 10% significance level (highlighted by blue areas in Fig. 2.7d).

2.5.3 Simulation of the Influence of TBO on Mid-tropospheric CO_2

I use the MOZART-2 model to investigate the TBO signal in the model mid-tropospheric CO_2. The AIRS mid-tropospheric CO_2 weighting function is applied to MOZART-2 CO_2 vertical profiles and the weighted MOZART-2 CO_2 is averaged over 5°S–20°N, 100°E–150°E in JJAS from 1991 to 2008. Figure 2.8a represents the time series of MOZART-2 detrended mid-tropospheric CO_2 concentration averaged over 5°S–20°N, 100°E–150°E in JJAS and detrended Indian monsoon rainfall index calculated from GPCP from 1991 to 2008. MOZART-2 mid-tropospheric CO_2 is highly correlated with the Indian monsoon rainfall index: the correlation coefficient is 0.56 (4% significance level).

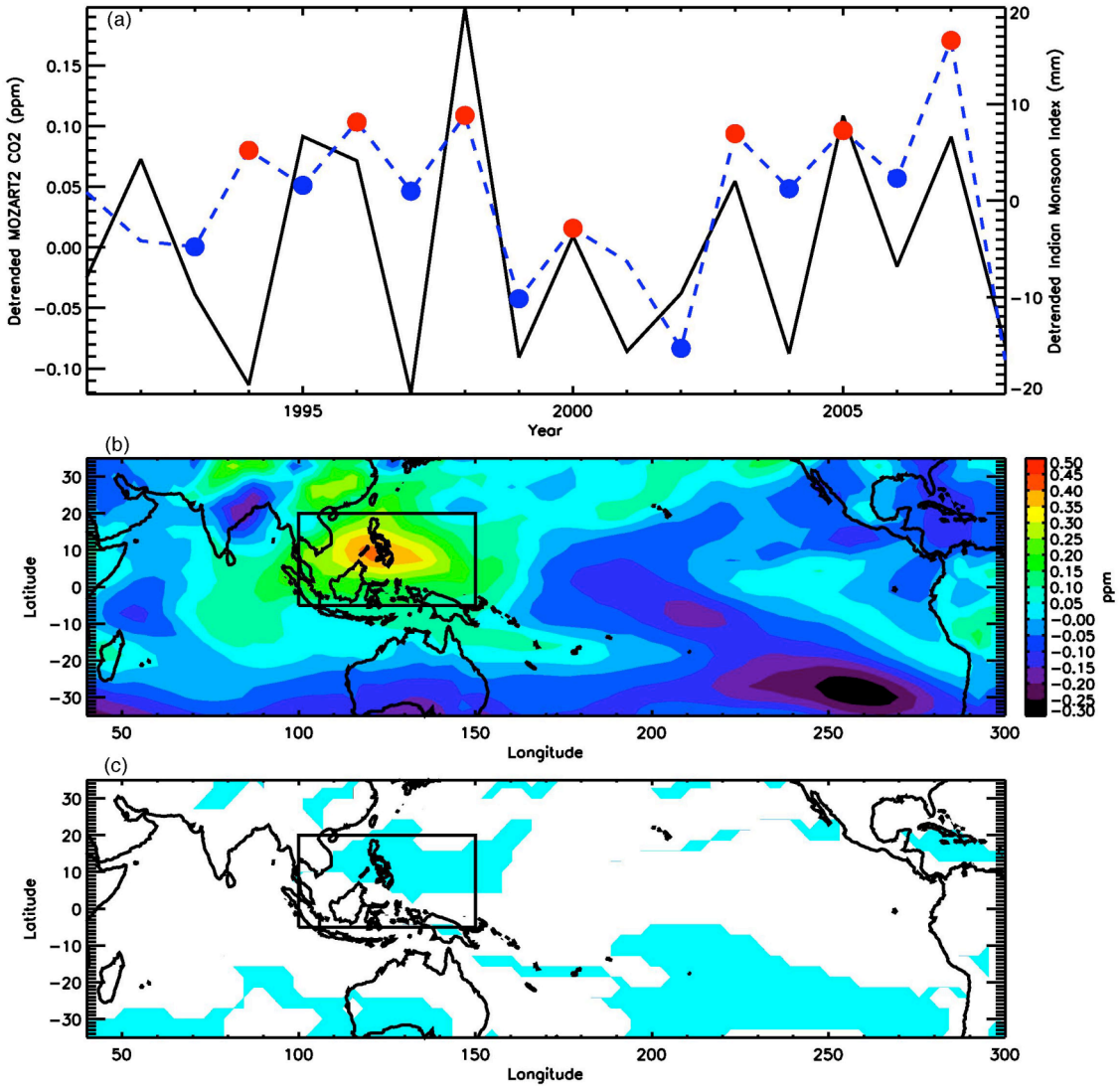

Figure 2.8. (a) MOZART-2 detrended mid-tropospheric CO_2 averaged at 5°S–20°N, 100°E–150°E (black solid line) and detrended Indian monsoon index derived from GPCP precipitation data (blue dashed line); correlation coefficient between two time series is 0.56 (4%). (b) MOZART-2 CO_2 differences between strong monsoon years (1996 and 2007) and weak monsoon years (1999 and 2002) in JJAS. (c) MOZART-2 CO_2 differences within 10% significance level highlighted in blue.

I selected two strong monsoon years (1996 and 2007) and two weak monsoon years (1999 and 2002) from the MOZART-2 model to investigate the influence of the TBO on the mid-tropospheric CO_2. MOZART-2 mid-tropospheric CO_2 differences between

strong and weak monsoon years demonstrate that there is more mid-tropospheric CO_2 over the Indo-Pacific area during strong monsoon years (Figure 2.8b). This is similar to the analysis using the AIRS mid-tropospheric CO_2. However, the difference amplitude of the AIRS mid-tropospheric CO_2 is smaller that of the MOZART-2. Jiang *et al.* (2008a, 2008b) found that the 3-D chemistry-transport models (MOZART-2 and GEOS-Chem) underestimated the amplitude of the seasonal cycle of CO_2 in the mid-troposphere as seen in the aircraft data, which is consistent with results found in the column-averaged CO_2 by Yang *et al.* (2007). Jiang *et al.* (2008a, 2008b) also found that the convective mass flux, which is very important for the correct simulation of CO_2 in the mid-troposphere, tend to be too weak in the model. This may be the same reason for the underestimation of the simulated TBO signal in the MOZART-2.

2.6 Conclusions

This work reveals for the first time that the concentration of the mid-tropospheric CO_2 can be influenced by the strength of the monsoon. The relationship between the TBO and variations of mid-tropospheric CO_2 concentrations over the Indo-Pacific region is established. The time series of AIRS mid-tropospheric CO_2 correlates well with the TBO index, showing that during strong monsoon years, there is more CO_2 in the mid-troposphere over Indonesia due to the strong Western Walker Cell, and vice versa. This suggests that the strength of the circulation influences CO_2 concentrations in the mid-troposphere. MOZART-2 mid-tropospheric CO_2 results are consistent with those from the observations, although the signal simulated in the model is smaller than that from AIRS CO_2, indicating that TBO might not have been fully represented in the model. The

correct identification of this natural variability of CO_2 is important for inferring the sources, sinks, and transport of CO_2. In addition, as the quality and quantity of satellite CO_2 data improves (Boesch *et al.*, 2011), modeling the variations in the mid-tropospheric CO_2 as a response to monsoon will continue to offer a unique opportunity to diagnose deficiencies in chemistry-transport models.

2.7 Acknowledgments

The author specially acknowledge Alexander Ruzmaikin and Runlie Shia, who gave helpful comments on this research.

Chapter 3

The Variation of Polar CO_2 during Sudden Warming

3.1 Introduction

The polar regions are very important to the climate change. The processes in the polar regions influence the climate at all latitudes and are thought to be particularly sensitive to climate change (IPCC, 2001; Räisänen, 2001; Holland and Bitz, 2003). Since most of Earth's snow and ice are in the polar regions, these area are expected to be the most affected by the snow/ice - surface albedo feedback effect (Curry and Schramm, 1994). Therefore, if the increased atmospheric CO_2 concentration causes global warming, the polar regions should warm faster than other locations on Earth due to changing surface albedo projections (IPCC, 2001; Räisänen, 2001; Holland and Bitz, 2003). Observations at the polar regions are so limited, however, and there are many uncertainties in determining the large-scale dynamics there.

The global distributions of chemical species retrieved from the Atmospheric Infrared Sounder (AIRS) offers a new opportunity to study the large-scale dynamics in the polar region. Since Sudden Stratospheric Warmings (SSWs) dominate the variability

of the wintertime stratospheric circulation in the polar regions, many researchers have studied the SSWs in order to understand large-scale dynamics of this area. Limpasuvan *et al.* (2004) have characterize five stages of SSW life cycle by studying the 39 SSW events in 44 years. Jiang *et al.* (2010) investigated the influence of stratospheric final warming on the upper tropospheric tracers, such as CO_2 and O_3 retrievals from AIRS (Chahine *et al.,* 2005; 2008). Shia *et al.* (2006) suggested that stratosphere-troposphere exchange might have a significant influence on the upper tropospheric CO_2 at high latitudes. The stratospheric warming events reflect a strong and clear coupling between the stratosphere and troposphere. In this chapter, I investigate the influence of SSW on the AIRS mid-tropospheric CO_2, focusing mainly on one SSW event, which occurred in March 2005.

3.2 Data

In addition to the AIRS (Aqua) satellite CO_2 retrievals, this chapter employs data from NCEP-2. NCEP-2 reanalysis data is a joint product from the National Centers for Environmental Prediction (NCEP) and the National Center for Atmospheric Research (NCAR). These are global data incorporating observations and numerical weather prediction (NWP) model output dating back to 1948. The data include near surface meteorological fields (temperature, geopotential height, winds u/v), and surface fluxes. The resolution is 2.5°×2.5°, in 17 levels from 1000 hPa to 10 hPa. The data are documented online.[1]

[1] Available at: http://wesley.wwb.noaa.gov/ reanalysis2/index.html

3.3 Stratospheric Sudden Warming

According to the World Meteorological Organization (WMO) definition, a stratospheric warming occurs when the latitudinal gradient in 10-hPa zonal-mean temperatures between 85°N–60°N is positive for more than five days. If the 10-hPa zonal wind at 65°N is concurrently easterly, the warming event is categorized as a ”major warming; otherwise, the warming event is categorized as ”minor warming”.

One such stratospheric warming, the “final warming” is that which occurs at the end of the winter, associated with the breakdown of the polar vortex. In the southern hemisphere, it occurs in November/December. In the north hemisphere, the final warming will happen as early as March and as late as May (Hardiman *et al.,* 2011). The final stratospheric warmings are related to the polar ozone content and the stratospheric circulation (Waugh and Rong, 2002).

3.4 Northern Hemisphere Annular Mode (NAM) Index

The annular modes are hemispheric scale patterns of climate variability, which are the most important patterns of climate variability in the middle and high latitudes. There are two kinds of annular modes in Earth's atmosphere: the Northern annular mode (NAM) and Southern annular mode (SAM) (Limpasuvan and Hartmann, 1999). Since it is related closely to the North Atlantic Oscillation, NAM is also referred to as the “Arctic Oscillation” (Thompson and Wallace, 1998; 2000). NAM’s structure covers the larger part of the Arctic, and its variability is more closely related to surface air temperature fluctuations over the Eurasian continent. The annular modes are able to explain variance

of week-to-week, month-to-month, or year-to-year in the extra-tropical atmospheric flow. It is not associated with the seasonal cycle.

The annual modes (NAM/SAM) is the first empirical orthogonal function (EOF) of geopotential height, and represent an important tool in the study of winter hemisphere variability (Thompson and Wallace, 1998; 2000).

EOF is also known as principal component analysis (PCA), which can be summarized as the following equation:

$$z(x,t) = \sum_{1}^{n} a_k(t) f_k(x) \qquad (3.1)$$

where Z is the original function of space and time. By the PCA method, the original data Z can be decomposed into two functions: the time function a, the principal component (PC) time series, and space function f, the empirical orthogonal function (EOF). EOF1 (f_1) represents the spatial pattern for the leading mode of geopotential height (GPH). PC1 (a_1) refers to the leading PC time series of GPH, which is also called the "NAM index".

The strength of the polar vortex is characterized by the NAM index, defined as the leading principal component time series of geopotential heights (Baldwin and Dunkerton, 2001).

3.5 Eliassen-Palm Flux and Divergence

Since Eliassen and Palm's paper (1961) on the Eliassen-Palm (EP) flux, EP fluxes have been utilized to investigate the wave activities in the middle and upper troposphere.

EP flux is very useful to study the evolution of the tropospheric and stratospheric jet and their interactions with the transient eddies. It helps diagnose both the wave propagation and wave-mean flow interaction.

EP flux can be calculated using the following equation (Andrews *et al.,* 1987):

$$F \equiv (0, \ -\rho_0 \overline{v'u'}, \ \rho_0 f_0 \frac{\overline{v'\theta'}}{\partial\theta_0 / \partial z}) \qquad (3.2)$$

$$v' = v - \bar{v}$$
$$u' = u - \bar{u}$$

where $\rho_0 = \rho_0(z)$ is the air density, $\theta_0 = \theta_0(z)$ is the potential temperature, the Coriolis parameter is $f_0 = 2.\Omega.\sin\varphi$ ($\Omega = 7.292 \times 10^{-5}$ rad/s), u and v are the horizontal and meridional velocities, and u' and v' the perturbations for the zonal and meridional winds.

EP flux divergence can be used to study the regions with a considerable eddy activity, quantify the acceleration (deceleration) of the internal forcing in the mean zonal flow, understand the contribution of the different zonal wave number in the eddy activity, and find the link between eddy forcing and baroclinic instability.

Divergence of the EP flux can be represented thus (Andrews *et al.*, 1987):

$$\nabla \bullet F = \frac{1}{\rho_0 a \cos\theta}\left[-\frac{\partial\left(\rho_0 \overline{v'u'}\right)}{\partial y} + \frac{\partial(\rho_0 f_0 \overline{v'\theta'}/\theta_{0z})}{\partial z}\right] \qquad (3.3)$$

$$
\begin{aligned}
&1)\ \nabla \bullet F > 0 \ \Rightarrow\ \frac{\partial \bar{u}}{\partial t} > 0 \ \Rightarrow\ \bar{u} \uparrow \ \text{, westerly wind} \uparrow \\
&2)\ \nabla \bullet F < 0 \ \Rightarrow\ \frac{\partial \bar{u}}{\partial t} < 0 \ \Rightarrow\ \bar{u} \downarrow \ \text{, westerly wind} \downarrow
\end{aligned}
\qquad (3.4)
$$

where $\nabla \cdot F$ is the EP flux divergence, and a is the earth's radius. Equations 3.4 show that when the EP flux divergence is positive, the westerly wind in the polar vortex increases, and when it is negative, the westerly wind decreases. EP flux can help diagnose the development/decay of SSWs. That is to say, when the EP flux divergence is positive, the polar vortex will enhance due to the increasing of the westerly wind; and when the EP flux divergence is negative, the westerly wind decreases or even switches into an easterly, and the polar vortex contracts or even collapses.

3.6 Influence of SSW on the Mid-tropospheric CO_2

I chose one SSW event in March 2005 to study the influence of SSW on the mid-tropospheric CO_2.

Figure 3.1 shows the leading EOF of NCEP-2 GPH at (a) 850 hpa, (b) 500 hpa, (c) 100 hpa, and (d) 30 hpa. For all four layers, GPH is low in the polar region and high in the mid-latitudes. Figure 3.2 is the leading PC time series of GPH (NAM index) as a function of altitudes from January 1, 2005 to May 31, 2005. The strength of the polar vortex is characterized by the NAM index. Positive (negative) NAM values represent a strong (weak) polar vortex. As shown in Figure 3.2, the NAM was positive in the stratosphere in the first two months of 2005. On the 71th day (March 12, 2005) it turned

into negative, which means that the stratospheric polar vortex collapsed. At the same time, the value of the NAM in the troposphere was negative, which suggests a nice coupling between the stratosphere and troposphere. Twelve days later (the 84th day of 2005), the polar vortex briefly returned and then the final warming occurred. After the final warming, the polar vortex would shrink and be destroyed. The SSW has important impact on the distribution of trace gases.

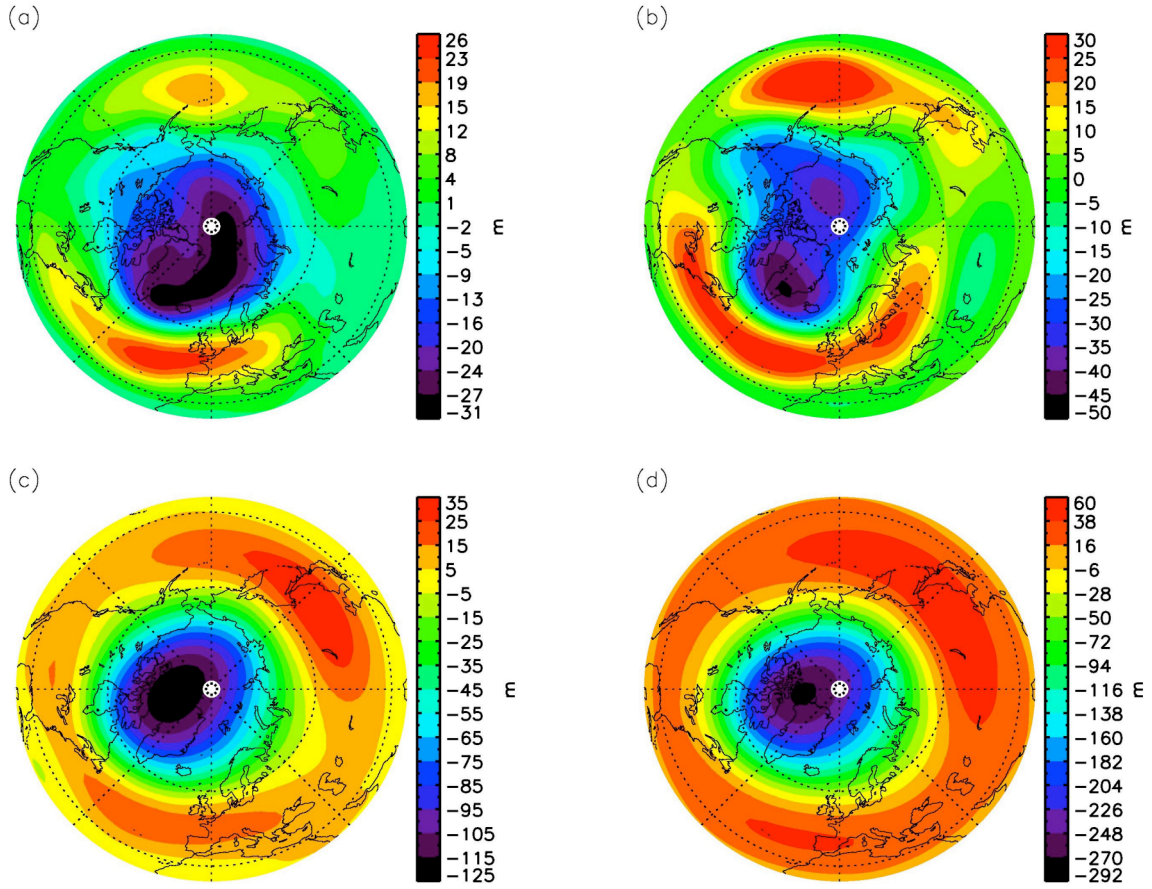

Figure 3.1. Spatial patterns of NCEP-2 geopotential height's leading mode in (a) 850 hPa, (b) 500 hPa, (c) 100 hPa, and (d) 30 hPa. Units: meter.

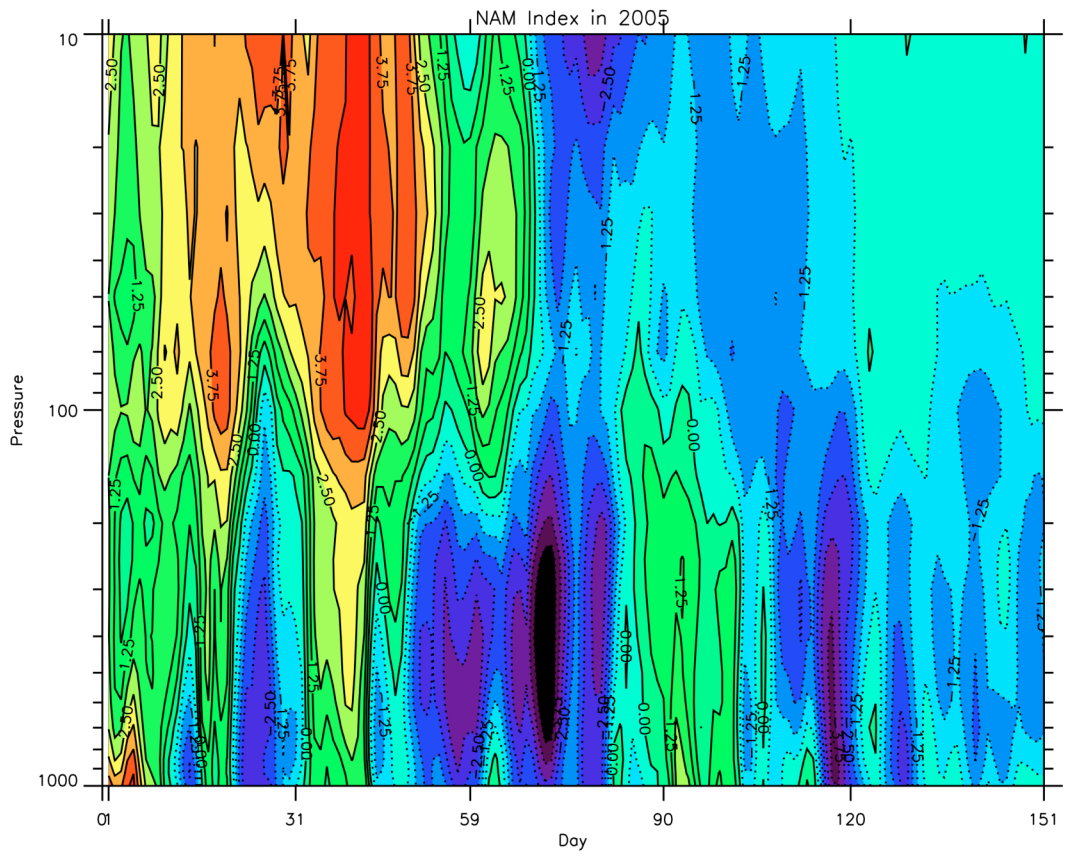

Figure 3.2. Vertical structure of Northern Annular Mode (NAM) index derived from NCEP-2 geopotential height spanning January 1, 2005 to May 31, 2005.

In order to further discuss the development of the SSW, EP flux was calculated using NCEP data. Mean values of EP-flux and EP-flux divergences before the SSW (Days 64–71 in 2005) and after (Days 83–87) are shown in Figure 3.3. The solid (dotted) contours referred to the positive (negative) EP flux divergences. In the northern hemisphere high latitudes (60°N–80°N) between 20 km to 30 km, and the mean values of EP flux divergences were negative before the SSW. From Equation 3.4 (2), the westerly winds would decrease. As a result, the polar vortex would be weakened. After the SSW, the

mean values of EP flux divergences were positive, which suggested that the westerly would increase and the polar vortex would become stronger.

Figure 3.4 shows the zonal mean winds before SSW (Days 64–71 in 2005), during SSW (Days 72–82 in 2005), and after SSW (Days 83–87 in 2005). In the stratosphere polar region (60°N–90°N, 20–30 km), the winds were westerly before the SSW, and switched to easterly during the SSW, at speeds of up to -12m/s. After the SSW and before the final warming, the easterly wind decreased. According to the definition of SSW from WMO, this SSW was a major SSW. Variations of the winds were consistent with the results from the EP flux and EP-flux divergences (Figure 3.3).

Figure 3.5 shows the mean values of horizontal zonal winds. Before the SSW, from 60°N to 80°N, the winds were westerly and the wind speeds were up to 65 m/s. During SSW days, the wind switched into easterly and the highest speed was about -30 m/s.

Figure 3.6 demonstrates the vertical distribution of the zonal mean temperature before SSW (Days 64–71 in 2005), during SSW (Days 72–82 in 2005), and after SSW (Days 83–87 in 2005) from NCEP2 reanalysis data. Before the SSW, the stratosphere temperature was low. The coldest temperature was 208 K, and the coldest center was at 85°N. The temperature decreased with altitudes from 60°N to 85°N. When SSW occurred, there was a warm center in the upper stratosphere and the temperature was up to 232 K. The temperature increased 20 K after the SSW. The SSW lasted for about ten days. After SSW, the warm temperature propagated downward to 20 km, and then decreased to 228 K.

(a)

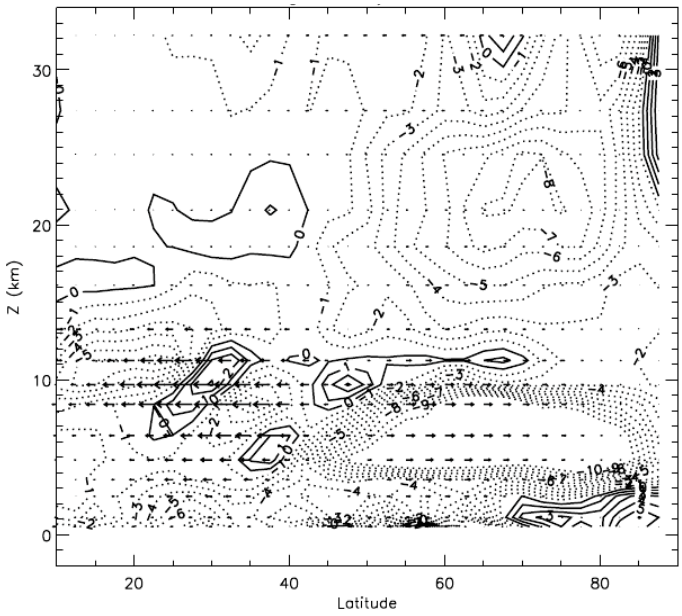

(b)

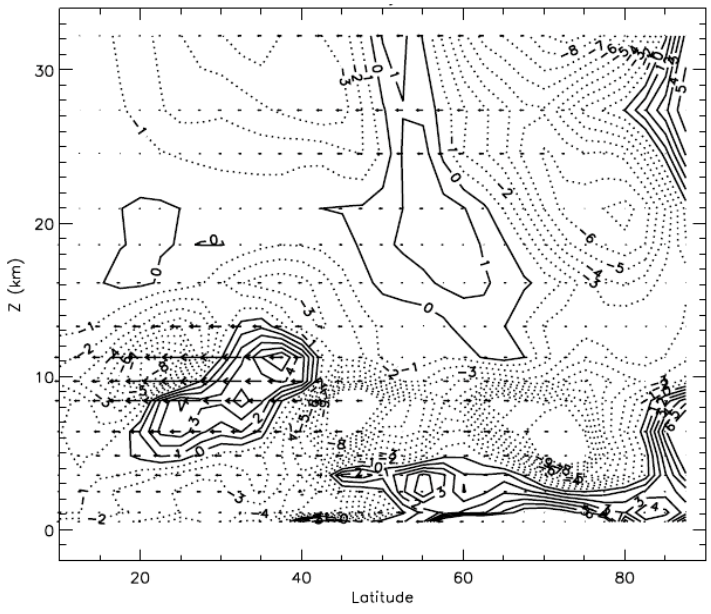

Figure 3.3. Mean values of EP-flux (a) before SSW (Days 64–71), and (b) after SSW (Days 83–87). Solid contours refer to positive EP-flux divergence; dotted contours refer to negative EP-flux divergence. Units for EP-flux: kg/s^2. Units for EP-flux divergence: m/s/day.

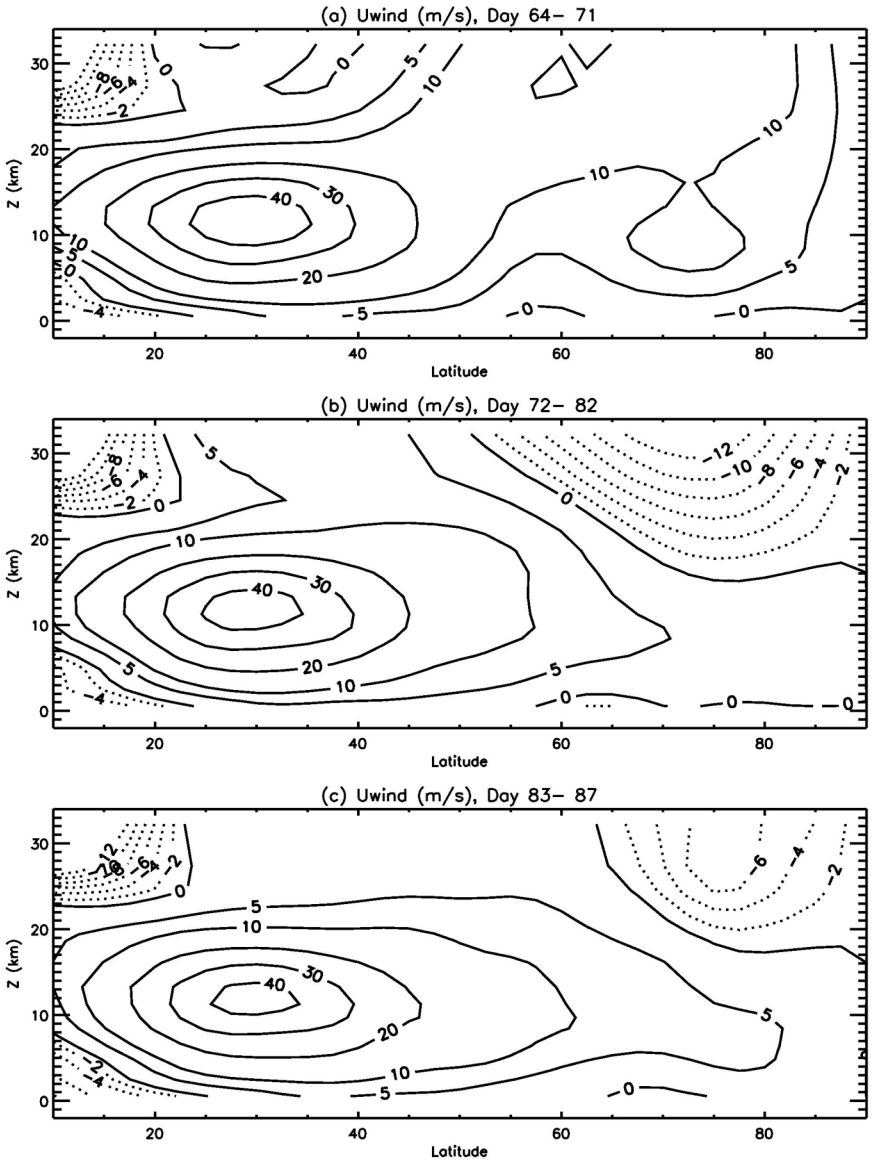

Figure 3.4. NCEP-2 zonal mean wind (a) before SSW (Days 64–71), (b) during SSW (Days 72–82), and (c) after SSW (Days 83–87). Solid contours refer to westerly winds; dotted contours refer to easterly winds. Units for zonal mean wind: m/s.

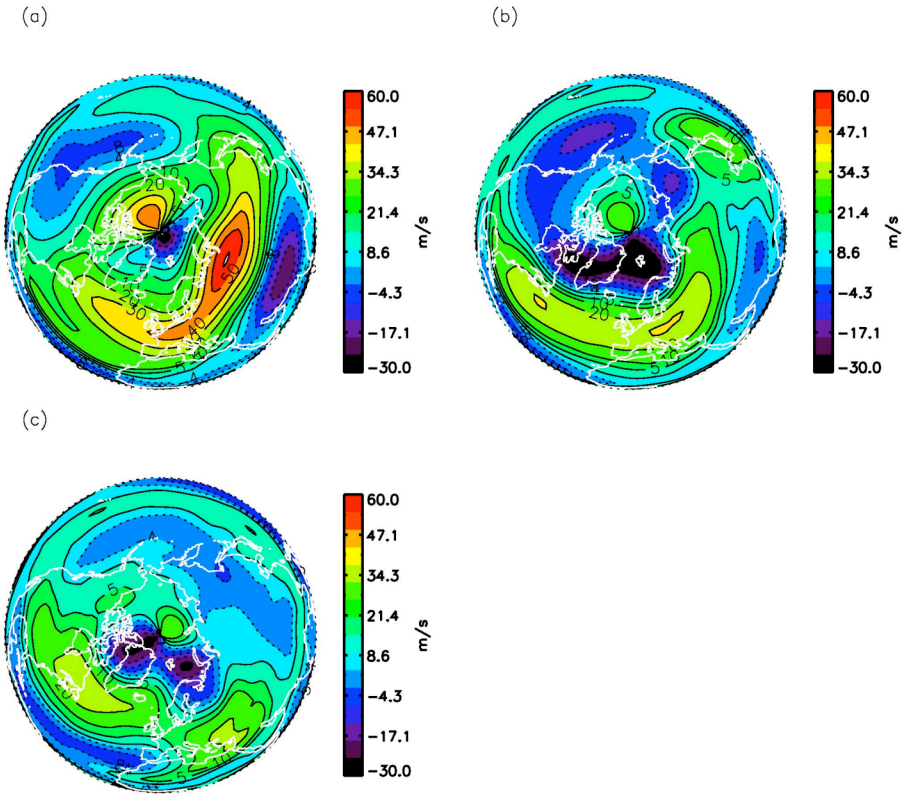

Figure 3.5. NCEP-2 30 hPa zonal winds (a) before SSW (Days 64–71), (b) during SSW (Days 72–82) and (c) after SSW (Days 83–87) in 2005. Units for zonal mean wind: m/s.

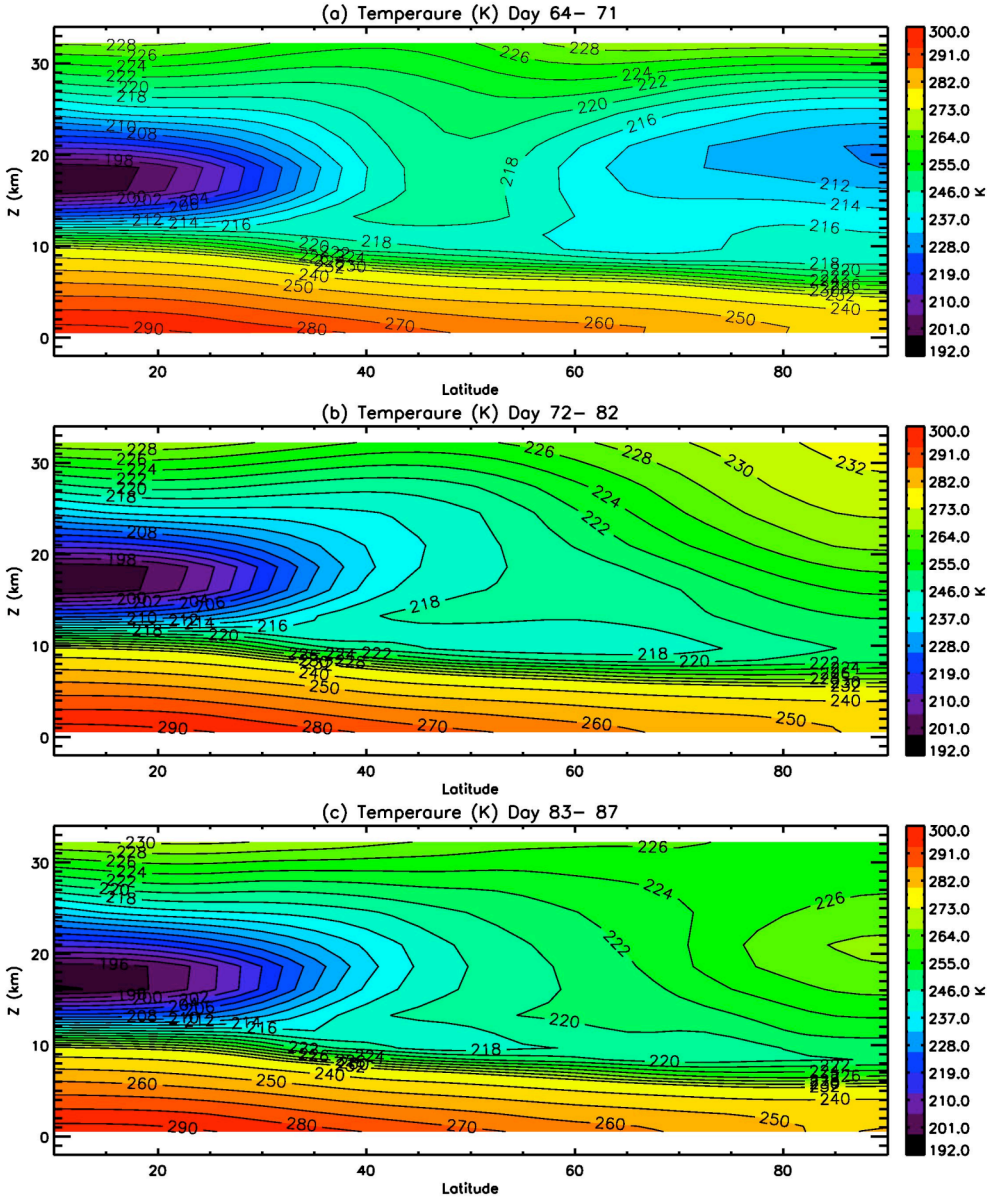

Figure 3.6. NCEP-2 zonal mean temperature (a) before SSW (Days 64–71), (b) during SSW (Days 72–82), and (c) after SSW (Days 83–87) in 2005. Units for temperature: K.

Figure 3.7 shows the horizontal distributions of 30 hPa NCEP-2 Temperature before SSW (Days 64–71), during SSW (Days 72–82), and after SSW (Dasy 83–87) in 2005. Before the SSW, there was a cold core in the polar region, and a warm band in the mid-latitude. When the SSW occurred, the warm band developed with the increase of the temperature and area. The cold core contracted. After the SSW, the warming core became weak and the cold core decayed. The gradients of temperature in the whole polar region decreased.

The time series of wind and temperature from the NCEP2 data can be used to identify the time for the SSW event. Figure 3.8a shows the NCEP-2 daily mean zonal wind (black) averaged for 60°N–80°N and temperature (green) averaged for 50°N–90°N. The winds turned into easterly on Mar 12, 2005. The polar wind changed direction from west to east between day 72 and 82, while the temperature increased by about 0.4 K. At the same time, CO_2 concentrations increased from 376 ppmv to 380 ppmv (Figure 3.8b). The winds returned to zero for about ten days after the first sudden warming. The polar vortex contracted and was destroyed after Mar 12, 2005. This process had an important impact on the CO_2. During these ten days, the temperature decreased back to the value it had before the SSW and CO_2 concentrations stayed at 380~380.5 ppmv. In April, the final warming occurred, the wind switched to east from day 90 to 150, and the tropospheric CO_2 concentrations increased during the whole of the month.

Mean values for the AIRS mid-tropospheric CO_2 mixing ratio before and after SSW are shown in Figure 3.9. Figure 3.9a shows the eight-day mean of AIRS mid-

tropospheric CO_2 concentrations and the geopotential heights before the SSW. The GPH decreased with the latitude and there was less CO_2 at the polar region before the SSW. After the SSW, the polar vortex areas shrank. Mid-latitude high concentrations of CO_2 were able to propagate to the polar region. As a result, the mean value of the AIRS mid-tropospheric CO_2 concentrations increased after the SSW (Figure 3.9b). In the vertical direction, the weakening of the polar vortex also lead to reduced sinking air in the center of the polar vortex. Less air with the lower CO_2 concentration from the upper layer would extend the increase in mid-tropospheric CO_2 concentrations. With both the horizontal and vertical effects, the polar mid-tropospheric CO_2 concentration becomes higher after the SSW than before.

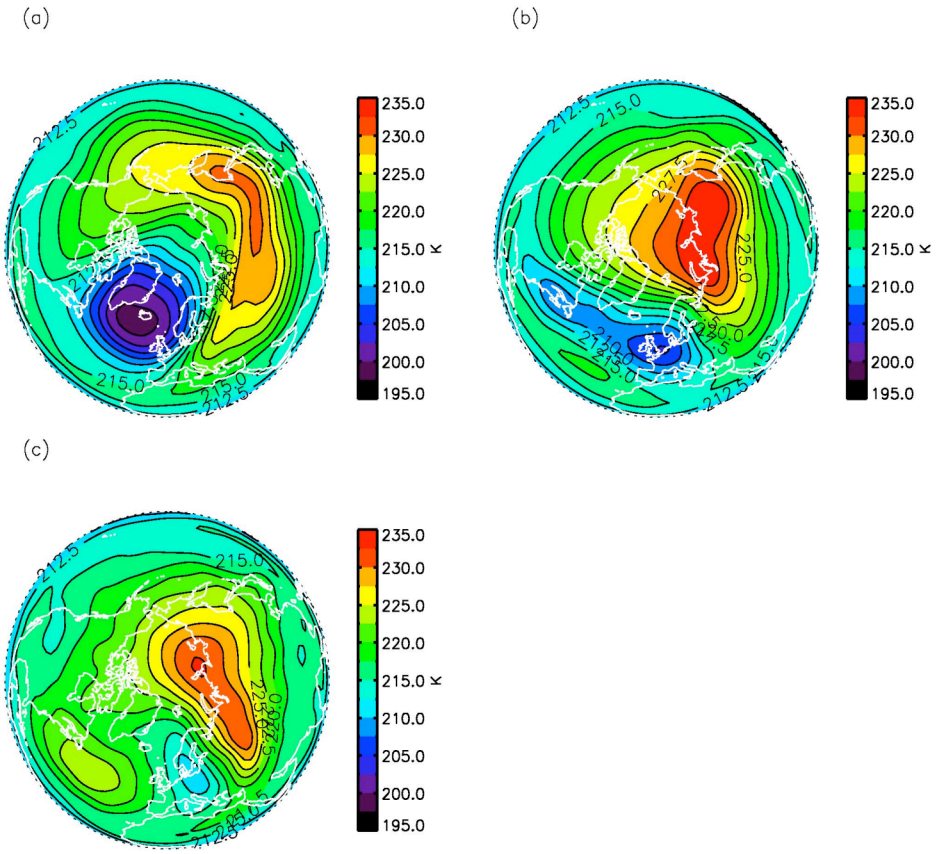

Figure 3.7. NCEP-2 30 hPa temperature (a) before SSW (Days 64–71), (b) during SSW (Days 72–82), and (c) after SSW (Days 83–87) in 2005. Units for temperature: K.

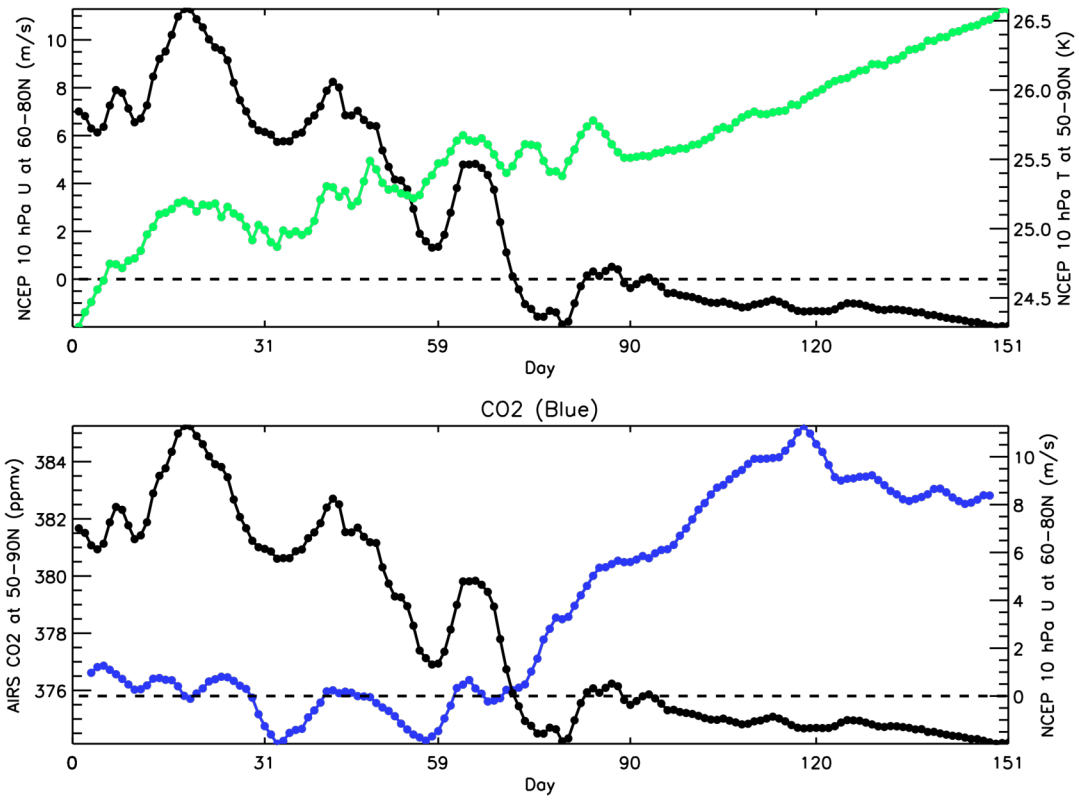

Figure 3.8. (a) Time series of NCEP-2 10 hPa daily mean horizontal wind averaged at 60°N–80°N (black line) and NCEP-2 10 hPa daily mean temperature averaged at 50°N–90°N (green line). (b) Time series of AIRS mid-tropospheric CO_2 mixing ratio averaged at 50°N–90°N (blue line). X-axis covers January 1, 2005 to May 31, 2005.

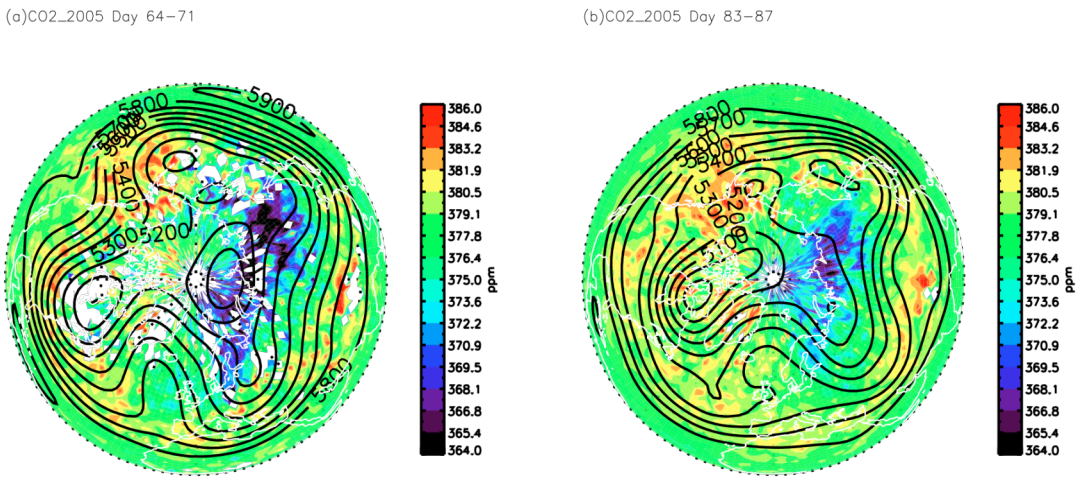

Figure 3.9. Mean values of (a) AIRS mid-tropospheric CO_2 mixing ratio averaged from March 5 to 12 (Days 64–71) in 2005, (b) AIRS mid-tropospheric CO_2 mixing ratio averaged from March 24 to 28 (Days 83–87) in 2005. Solid contours are the 500 hPa geopotential heights.

3.7 Conclusions

This chapter has studied one major SSW event that occurred in March, 2005. The SSW lasted for about eleven days (from day 72 to 82). Before the SSW, the wind was westerly and EP-flux divergence was negative. The CO_2 concentration was low in the polar region, and especially in the polar vortex center. During the SSW, the polar vortex became weak and eventually vanished, and the westerly wind switched to an easterly. The mean temperature increased by 2.5 K. The EP-flux divergence was positive after the SSW, and the easterly zonal wind decreased, while the westerly zonal wind increased.

The SSW has an influence on the mid-tropospheric CO_2 concentrations, which could be detected from the AIRS mid-tropopheric CO_2. After the SSW, the mean value of CO_2 concentrations in the polar region increased for about 2.5 ppmv. The polar vortex

areas shrank after the SSW, so the mid-latitude high concentrations of CO_2 was able to propagate to the polar region in the horizontal direction. After the SSW, the strength of the polar vortex was weakened, which was associated with reduced mixing between the stratosphere and troposphere. As a result, the mid-tropospheric CO_2 would have less contamination from the stratospheric low concentrations of CO_2. The mid-tropospheric CO_2 concentrations would also increase after the SSW, taking into account the effect in the vertical direction. In summary, the mid-tropospheric polar CO_2 concentrations increase after the SSW, which is very important for a better understanding of the influence of large-scale dynamics on CO_2 in the polar region.

Chapter 4

The Influence of El Niño on Mid-tropospheric CO_2 from MOZART-2 Model

4.1 Introduction

CO_2 seasonal cycle amplitudes are closely related to the carbon sequestration in the biosphere (Pearman and Hyson, 1980, 1981; Cleveland *et al.*, 1983; Bacastow *et al.*, 1985; Keeling *et al.*, 1996; Buermann *et al.*, 2007). Atmospheric CO_2 demonstrates not only the annual cycle, but also intra-seasonal and inter-annual variabilities (Bacastow, 1976; Enting, 1987; Feely *et al.*, 1987; Keeling and Revelle, 1985; Keeling *et al.*, 1995; Dargaville *et al.*, 2000; Dettinger and Ghil, 1998; Jiang *et al.*, 2010). From the satellite/in-situ observations and model simulations, there are Madden-Julian Oscillation (MJO) and semi-annual oscillation (SAO) signals in the middle tropospheric CO_2 (Li *et al.*, 2010; Jiang *et al.*, 2012). Jiang *et al.* (2010) has found that El Niño and Southern Oscillation (ENSO) can also influence the mid-tropospheric CO_2 concentration in Atmospheric Infrared Sounder (AIRS) mid-tropospheric CO_2 data. Mid-tropospheric CO_2 is enhanced in the central Pacific Ocean and reduced in the western Pacific Ocean during El Niño (Jiang *et al*., 2010). In the high latitudes, mid-tropospheric CO_2 concentration can be influenced by the strength of the polar vortex (Chapter 3). In this chapter, the

MOZART-2 model is used to investigate the influence of El Niño on the mid-tropospheric CO_2.

4.2 Model

In this chapter, I use the three-dimensional (3-D) chemistry transport model, Model of Ozone and Related Chemical Tracers version 2 (MOZART-2), to investigate the El Niño signal in the model mid-tropospheric CO_2 (see Section 3.2 for details on MOZART-2).

4.3 Results

Jiang *et al*. (2010) calculated the difference of CO_2 between El Niño and La Niña months. They found that there are more (less) CO_2 in the central Pacific and less (more) CO_2 in the western Pacific during El Niño (La Niña) as a result of changes in the Walker circulation (Jiang *et al*., 2010). In order to investigate the temporal variability of mid-tropospheric CO_2 as a response to the ENSO, a chemistry-transport model is used to simulate the ENSO signal in the mid-troposphere. MOZART-2 convolved mid-tropospheric CO_2 difference between central Pacific and western Pacific regions was calculated. The detrended MOZART-2 CO_2 difference is shown in Figure 4.1a. The detrended model CO_2 difference correlates well with the inverted and detrended SOI index. The correlation coefficient between two time series is 0.44 (1%). A lowpass filter was applied to the detrended MOZART-2 mid-tropospheric CO_2 difference and the inverted and detrended SOI. The correlation coefficient between two low-pass filtered time series is 0.63 (1%).

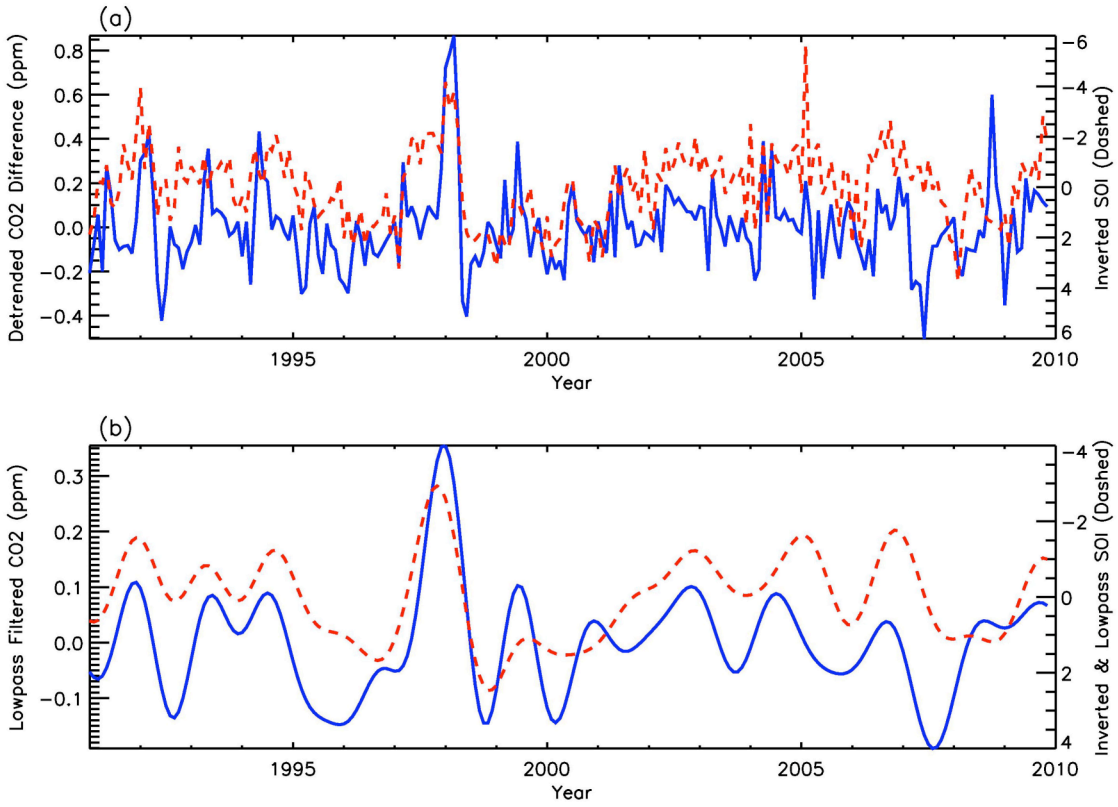

Figure 4.1. (a) Detrended MOZART-2 mid-tropospheric CO_2 difference between central Pacific (180°E–220°E; 10°S–14°N) and western Pacific (100°E–140°E, 10°S–14°N) (blue solid line) and inverted and detrended Southern Oscillation Index (red dashed line). Correlation coefficient between two time series is 0.44 (1%). (b) Detrended and lowpass filtered MOZART-2 CO_2 difference (blue solid line) and inverted, detrended, and lowpass filtered SOI (red dashed line). Correlation coefficient between two lowpass filtered time series is 0.63 (1%).

I used the SOI to separate MOZART-2 detrended and deseasonalized CO_2 into two groups. When the SOI was 1.5 standard deviations below (above) the mean value, I considered it an El Niño (La Niña) month. MOZART-2 detrended and deseasonalized CO_2 data averaged for 13 El Niño months is shown in Figure 4.2a. I also have overlain the vertical velocity in Figure 4.2a. During El Niño months, there is rising air over the Central Pacific Ocean as shown by the dotted white contours in Fig. 4.2a. As a result, the surface high CO_2 can be lifted into the middle troposphere over the Central Pacific region

during the El Niño months. Low concentration of mid-tropospheric CO_2 is seen in the Western Pacific Ocean. However, the low CO_2 appears in the subtropical area instead of tropical area as seen in the AIRS mid-tropospheric CO_2 (Jiang *et al.*, 2010), which might be related to the relatively weak vertical velocity and relatively strong northward winds over the Western Pacific Ocean in the ECMWF-Interim Reanalysis data. In Fig. 4.2b, MOZART-2 detrended and deseasonalized CO_2 data for 14 La Niña months suggest that lower CO_2 has been transported from high altitude to the mid-troposphere over the Central Pacific Ocean. High CO_2 is seen over the western Pacific Ocean; however, the position for the high CO_2 shifts a little bit north, which might be related to the relatively strong northward winds in the model. Fig. 4.2c presents the difference of MOZART-2 mid-tropospheric CO_2 between El Niño and La Niña months. The difference, (El Niño - La Niña), of MOZART-2 mid-tropospheric CO_2 is about 1 ppm over the Central Pacific and -0.7 ppm over the Western Pacific. This is consistent with changes in the Walker Circulation during El Niño and La Niña events. A Student-t test was used to calculate the statistical significance of the difference for MOZART-2 CO_2 concentration in El Niño and La Niña events. The CO_2 difference between El Niño and La Niña events were statistically significant when t was larger than a certain value t_0. CO_2 differences with significance levels less than 5% are highlighted by blue areas in Fig. 4.2d.

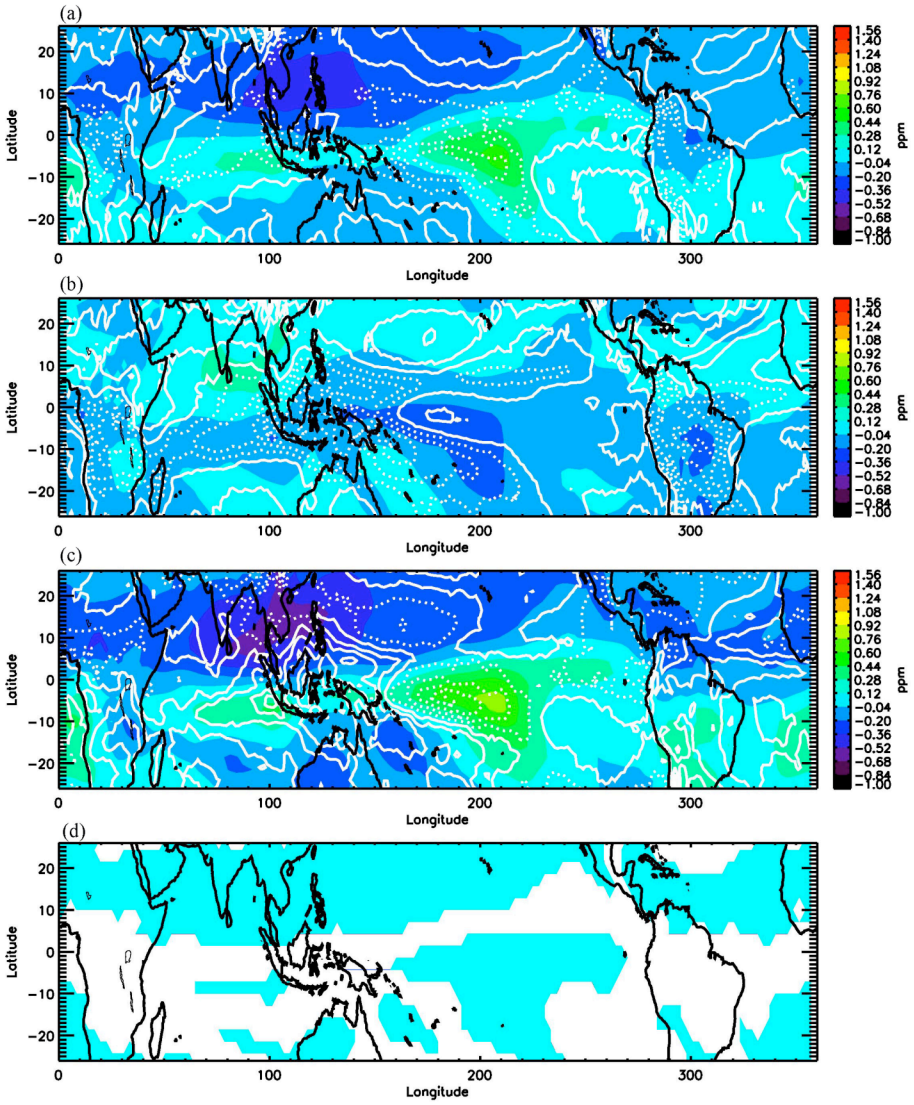

Figure 4.2. (a) MOZART-2 detrended and deseasonalized CO_2 (color) and vertical velocities (white contours) averaged for 13 El Niño months, (b) as (a) for 14 La Niña months, (c) MOZART-2 CO_2 difference and vertical velocity differences (white contours) between El Niño and La Niña months, (d) MOZART-2 CO_2 differences within 5% significance level highlighted in blue. Solid (sotted) white contours refer to the sinking (rising) air.

In order to better investigate the temporal and spatial variability of the ENSO signal in the MOZART-2 mid-tropospheric CO_2, I applied a multiple regression method to the MOZART-2 mid-tropospheric CO_2. I decomposed MOZART-2 mid-tropospheric CO_2 concentrations, X, at each location using the following empirical model (Prinn *et al.*, 2000; Jiang *et al.*, 2012):

$$\begin{aligned} X(t) = {} & A_0 + A_1 N P_1(t/N-1) + A_2 N^2 P_2(t/N-1) + A_3 N^3 P_3(t/N-1) \\ & + C_1 \cos(2\pi t) + S_1 \sin(2\pi t) + C_2 \cos(4\pi t) + S_2 \sin(4\pi t) + B \bullet S(t) \end{aligned} \quad (1)$$

where t is time; N is the half length of the time period; P_1, P_2, and P_3 are the first, second, and third Legendre polynomials. The coefficients A_0, A_1, A_2, and A_3 are the mean value, the trend, the acceleration in the trend, and the coefficient for P_3, respectively. I added the third Legendre function to better fit the data sets. Seasonal and semi-annual cycles are represented by the harmonic functions; C_1 and S_1 are the amplitudes of the annual cycle, while C_2 and S_2 are the amplitudes of the semi-annual cycle. B is the regression coefficient for the ENSO signal in the mid-tropospheric CO_2, and *S(t)* is the inversed, detrended, and normalized SOI index, which is shown in Fig. 4.3a. This is used for regressing the coefficients of ENSO signal in the MOZART-2 mid-tropospheric CO_2. The standard deviation for the inversed and normalized SOI is 1.

Figure 4.3b show the ENSO component in the MOZART-2 mid-tropospheric CO_2. There is more (less) mid-tropospheric CO_2 over the central (western) Pacific Ocean during El Nino months. The amplitude of the ENSO signal in the MOZART-2 mid-tropospheric CO_2 was about half of the ENSO amplitude in the AIRS mid-tropospheric CO_2. Additionally, comparing with the results from AIRS mid-tropospheric CO_2, the

spatial pattern of ENSO signal in the MOZART-2 was different in the western Pacific Ocean. These results can be improved in the future with better transport fields and surface emission inventories.

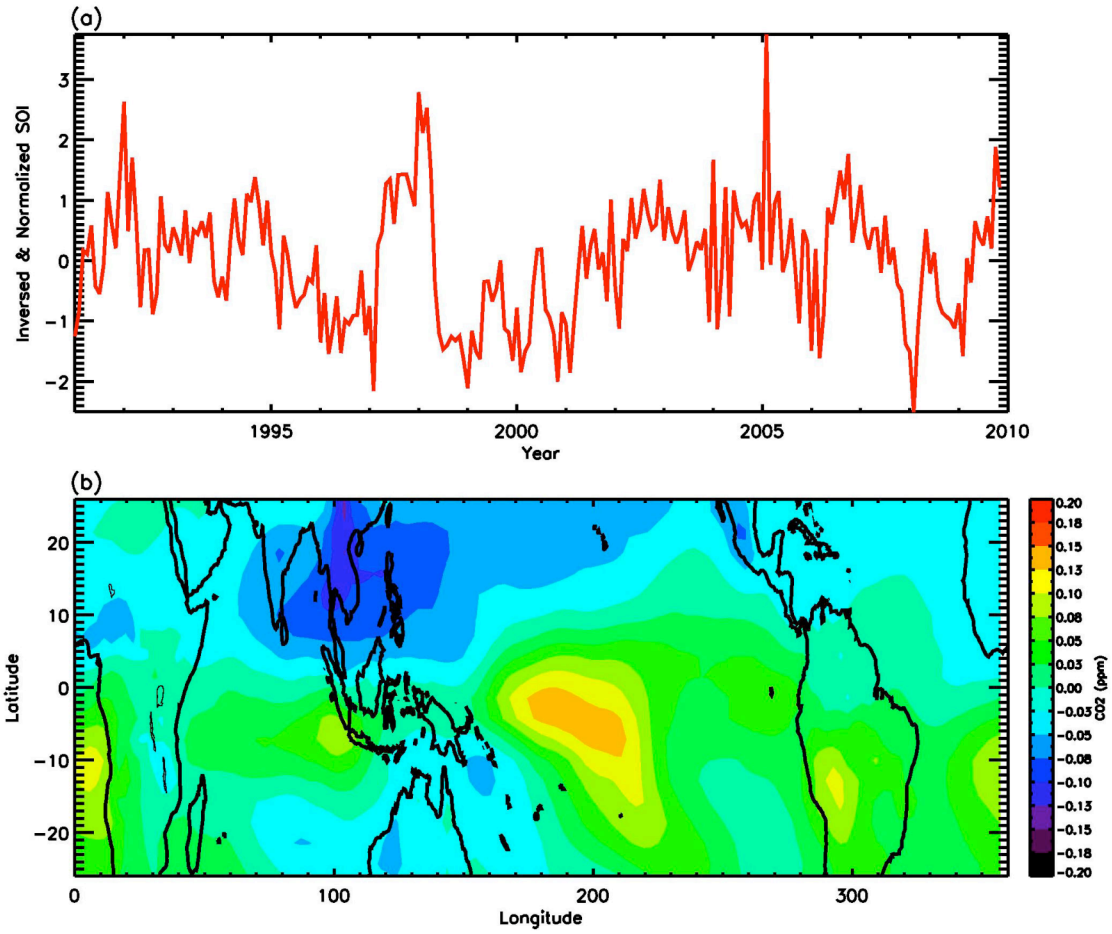

Figure 4.3. (a) Inversed, detrended, and normalized SOI index, (b) regression map of ENSO signal in MOZART-2 mid-tropospheric CO_2 in the tropics. Units: ppm.

4.4 Conclusions

I used the MOZART-2 model to investigate how well the model simulates the ENSO signal in the mid-tropospheric CO_2. A multiple regression method was applied to the MOZART-2 mid-tropospheric CO_2 in the tropical region. During El Nino episodes, there are more (less) model mid-tropospheric CO_2 in the central (western) Pacific as a result of changing in the Walker Circulation. This is consistent with the observations, although the amplitude and spatial pattern in the model was a little different compared with that in the AIRS mid-tropospheric CO_2. The results will be very helpful for modelers to better simulate ENSO signals in the middle troposphere and better constrain vertical transport in the chemistry-transport models in the future.

4.5 Acknowledgements

I especially acknowledge Dr. Moustafa Chahine and Dr. Alexander Ruzmaikin, who gave helpful suggestions on this research.

Chapter 5

El Niño-Southern Oscillation in Tropical and Mid-latitude Column Ozone

5.1 Introduction

The influence of El Niño-Southern Oscillation (ENSO) on the sea surface temperature (SST), surface pressure, winds, and convection is well known (*e.g.*, Trenberth and Shea, 1987; Trenberth, 1997). During El Niño events, temperature in the lower stratospheric is reduced in the tropics and increased in the Arctic (Garcia-Herrera *et al.*, 2006; Free and Seidel, 2009). Using a multiple regression method, Hood *et al.* (2010) have found that ENSO can influence ozone volume mixing ratios. Ozone anomalies are negative in the lower stratosphere and positive in the middle stratosphere during El Niño (Hood *et al.*, 2010). Chandra *et al.* (1998) and Thompson and Hudson (1999) also identified an ENSO signal in the tropospheric column ozone: tropospheric column ozone decreases in the eastern Pacific and increases in the western Pacific as a result of the eastward shift of the tropical convective activity (Chandra *et al.*, 1998).

ENSO also affects the total column ozone abundance (Bojkov, 1987; Shiotani, 1992; Zerefos *et al.*, 1992; Kayano, 1997; Kita *et al.*, 2000; Camp *et al.*, 2003; Cagnazzo

et al., 2009). Zerefos *et al.* (1992) found that ozone reductions in tropical regions could extend to middle and high latitudes following large El Niño events. Using the empirical orthogonal function (EOF) method, Kayano (1997) found that the first two modes of the total column ozone between 70º N and 70º S are related to ENSO. Kita *et al.* (2000) used total column ozone from the Total Ozone Mapping Spectrometer (TOMS) and found a significant increase of total ozone over Indonesia during El Niño periods, related to the decreased precipitation and extensive forest fires occurring in the dry season during the El Niño periods. Camp *et al.* (2003) used the total column ozone observed by TOMS and revealed that there is an ENSO signal in the fourth mode of the total column ozone in the tropical region. The power spectral estimate of the principal component (PC) time series for the fourth mode reveals that most signals are related to the ENSO signal in total column ozone.

There are negative total column ozone anomalies in the eastern tropical Pacific and positive total column ozone anomalies in the western Pacific during the El Niño events. The influence of ENSO on total column ozone can be explained by the variation in the tropopause height driven by changes of tropical deep convection and the changes of the Brewer-Dobson circulation (Schubert and Munteanu, 1988; Shiotani, 1992; Hasebe, 1993; Garcia-Herrera *et al.*, 2006; Free and Seidel, 2009). Such a causal relationship between total column ozone and the tropopause height is also evident in the Madden-Julian oscillation (Tian *et al.*, 2007). However, a quantitative demonstration of the impact of ENSO on total column ozone and tropopause height has not been carried out to date using model simulations.

In this chapter, I focus on the ENSO signal in the tropopause pressure and the total column ozone simulated by version 1 of the Goddard Earth Observing System Chemistry-Climate Model (GEOS CCM) (Pawson *et al.*, 2008). Principal component analysis (PCA) will be applied to model total column ozone and the spatial pattern of the modeled ENSO signal will be compared with that from Camp *et al.* (2003). I also investigate the mechanism for the 3.5-yr signal in mid-latitude total column ozone. The 3.5-yr signal was first found in the total column ozone observations from Arosa, Switzerland, and the same signal also appears in the first leading mode of the Northern Hemispheric total column ozone (Jiang *et al.*, 2008a). In this chapter, I investigate a possible relationship between the 3.5-yr signal and ENSO.

5.2 The GEOS Chemistry–climate Model and Data

The GEOS CCM (version 1) (Pawson *et al.*, 2008) integrates the GEOS-4 general circulation model with a stratospheric chemistry model (Douglass *et al.*, 2003; Stolarski *et al.*, 2006). Atmospheric composition and dynamics are coupled through radiative heating. In the model radiation module, three-dimensional constituent concentrations (CO2, O3, H2O, CH4, N2O, CFC-11, and CFC-12) vary as a function of time. The P1 model run of Pawson *et al.* (2008), to be analyzed in this study, spanned 54 years (1951–2004) at 2° (latitude) × 2.5° (longitude) with 55 layers between the surface and about 80 km. Zonal-mean fields from this run were also included in Cagnazzo *et al.* (2009). At the lower boundary, monthly mean SST and sea ice were prescribed from observations (Rayner *et al.*, 2003), along with time-dependent concentrations of greenhouse gases and chlorofluorocarbons (see Eyring *et al.*, 2006). Neither the solar cycle nor volcanic aerosol

variations were included in the model. This version of the model does not simulate a quasi-biennial oscillation (QBO) signal (see Horinouchi *et al.*, 2003). The signals of these three sources of ozone variability are therefore all absent from the simulation. To extract the ENSO signal in the GEOS CCM, two simulated monthly mean fields are examined: the tropopause pressure P_T and the total column ozone Ω_S. The former field is obtained using the lapse-rate definition tropopause (Sturman and Tapper, 1996). The latter is the integrated profile of the total amount of ozone in the atmosphere. A comparative analysis of the imposed monthly mean SSTs between 1951 and 2004 is also shown.

For comparison with the simulation, monthly mean total column ozone data from ground stations are analyzed (the data are available online).[2] Twenty-one stations with continuous records longer than 20yr are used, so as to include several complete cycles of the 3.5-yr ozone signal. The total column ozone time series from these stations is compared with the model simulation.

5.3 Methods

The filtering and analysis technique of Jiang *et al.* (2008a) was applied to the GEOS CCM model outputs, which are the gridded monthly means SST, P_T, and Ω_S. The mean annual cycle and the linear trend computed for the 54-year monthly time series were subtracted from the original time series to create detrended monthly anomalies. The mean annual cycle was calculated from the monthly mean fields for 54 years and the linear trend calculated as linear regression of the series. A spectral filter was then applied

[2] At: http://www.woudc.org/data_e.html

to these monthly anomalies to separate the interannual variability (IAV) from higher-frequency oscillations. As in Jiang *et al.* (2008a), the filter was constructed to extract signals at periods longer than 15 months by convolving a step function with a Hanning window, which has a high concentration in the central lobe and insignificant side lobes.

These time-filtered anomalies of GEOS CCM SST, P_T, and Ω_S were used in a PCA (Preisendorfer, 1988; Camp *et al.*, 2003) to extract the leading spatial EOFs and their associated time-dependent amplitudes (the PC time series). PCA can reduce the dimensionality of the original dataset, and small sets of orthogonal functions are much easier to understand and analyze (Dunteman, 1989). The EOFs are the orthogonal eigenfunctions of the covariance matrix of the dataset sorted by the decreasing values of associated eigenvalues. Since these eigenvalues represent the variance captured by each EOF, PCA guarantees that the leading EOFs capture more of the total variance of the dataset than any other orthogonal vectors. The observed total column ozone at different stations were deseasonalized and detrended before the power spectral analysis was applied. Spectral analysis was also applied to the modeled deseasonalized and detrended total column ozone. To obtain the statistical significance of signals in a power spectrum, the amplitudes of the spectral peaks were compared with a red noise spectrum (Gilman *et al.*, 1963). The 10% and 5% significance levels for the power spectrum were found using F statistics to compare the spectrum to the red noise spectrum.

5.4 ENSO Signals in Total Column Ozone

ENSO is very important in the tropical region. In order to study variations of SST, P_T, and Ω_S in the tropical region (25°S–25°N) during ENSO events, I use the PCA method to analyze the GEOS CCM results in the tropical region. The leading mode of the PCA of filtered tropical (25°S–25°N) anomalies captures 46.9%, 33.9%, and 63.8% of the total variance in GEOS CCM SST, P_T, and Ω_S, respectively (Table 5.1). The Southern Oscillation index (SOI; the sea level pressure difference between Tahiti and Darwin) is used to calculate the correlations between ENSO and leading PC time series (the SOI is

TABLE 5.1. Variances, spectral peaks, and correlations (lag = 0) for the first modes of the GEOS CCM SST, P_T, and Ω_S.

Mode	Variance captured	Spectral Peaks	Correlations (significance level)		
			Lowpass filtered SOI	SST (PC1)	P_T (PC1)
SST	46.9%	3.5-year; 5-year	0.88 (0.1%)	–	–
P_T	33.9%	17 months; 28 months; 3.5-year; 5-year	0.65 (0.1%)	0.72 (0.1%)	–
Ω_S	63.8%	17 months; 28 months; 3.5-year	0.53 (0.1%)	0.57 (0.1%)	0.82 (0.1%)

available online).[3] For a fair comparison, I applied a low-pass filter to the detrended SOI index. Comparison of the time series of the detrended and low-pass filtered SOI and the F1 amplitude of the first mode (PC1) of the SST (Fig. 5.1) reveals a good correlation, with in-phase variations. Note that negative (positive) SOI values denote the El Niño (La Niña) events. The correlation between the two time series is 0.88 and it is significant at

[3] At: http://www.cpc.noaa.gov/data/indices/soi

the 0.1% level. The significance level was computed by a Monte Carlo method (Press *et al.*, 1992): a small numerical value denotes high statistical significance. Time series of PC1 for P_T and Ω_S reveal a similar low-frequency oscillation as for low-pass filtered SOI, with some higher-frequency variations superimposed. This leads to somewhat lower correlations (0.65 and 0.53) between these time series and the low-pass filtered SOI, but they remain highly significant (see Table1). The correlation between PC1s of P_T and Ω_S is 0.82. The power spectra of the PC1s of SST, P_T, and Ω_S (Fig. 5.2) all show strong spectral peaks near 3–7 years, similar to those in ENSO. The higher-frequency variations evident in P_T and Ω_S also lead to prominent peaks near 17 months, which might be a beat frequency between the annual cycle and the ENSO signal.

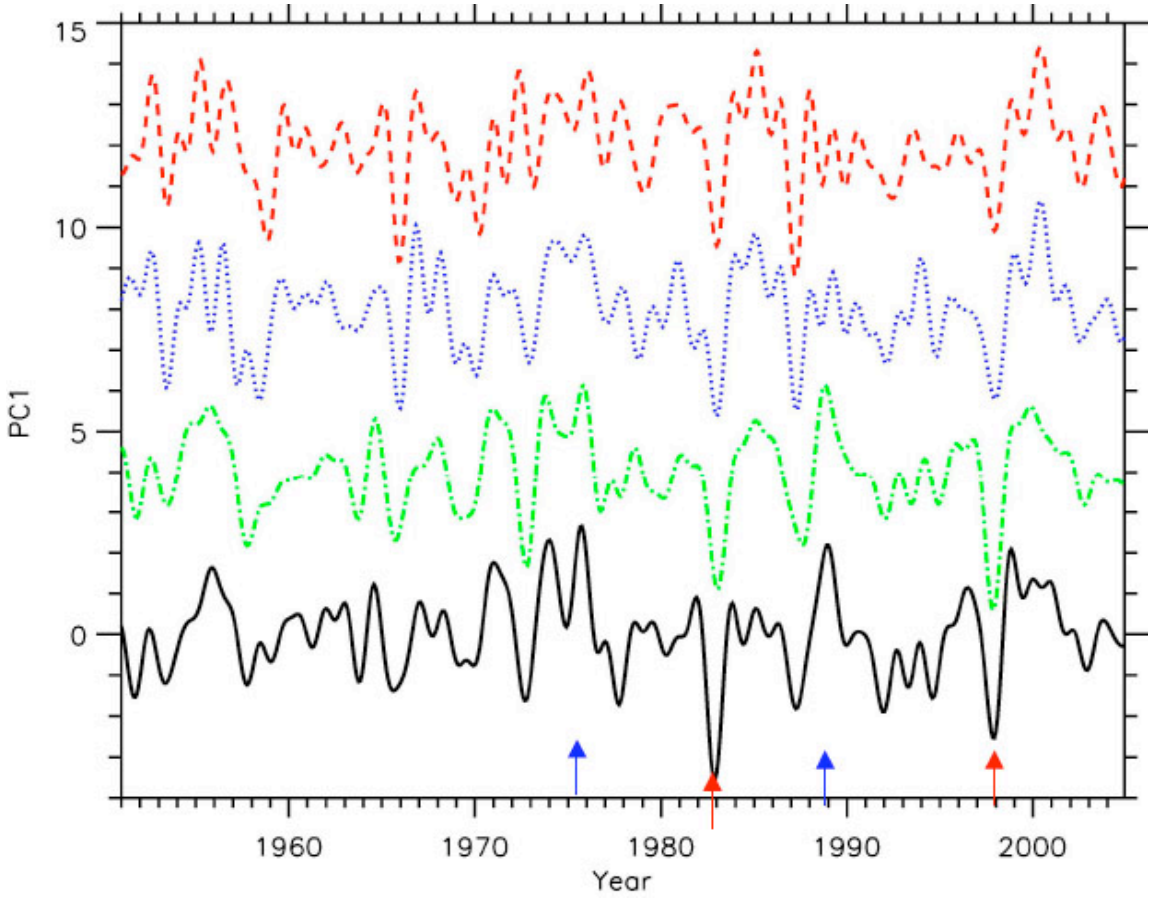

Figure 5.1. PC1 time series for first modes of GEOS CCM SST (green dashed-dotted line, shifted upward by 4), P_T (blue dotted line, shifted upward by 8), and Ω_S (red dashed line, shifted upward by 12). Low-pass filtered and detrended SOI index shown by a black solid line. Red (blue) arrows represent El Niño (La Niña) events. Correlation coefficients between SOI and SST, P_T, and Ω_S are 0.88, 0.65, and 0.53, respectively.

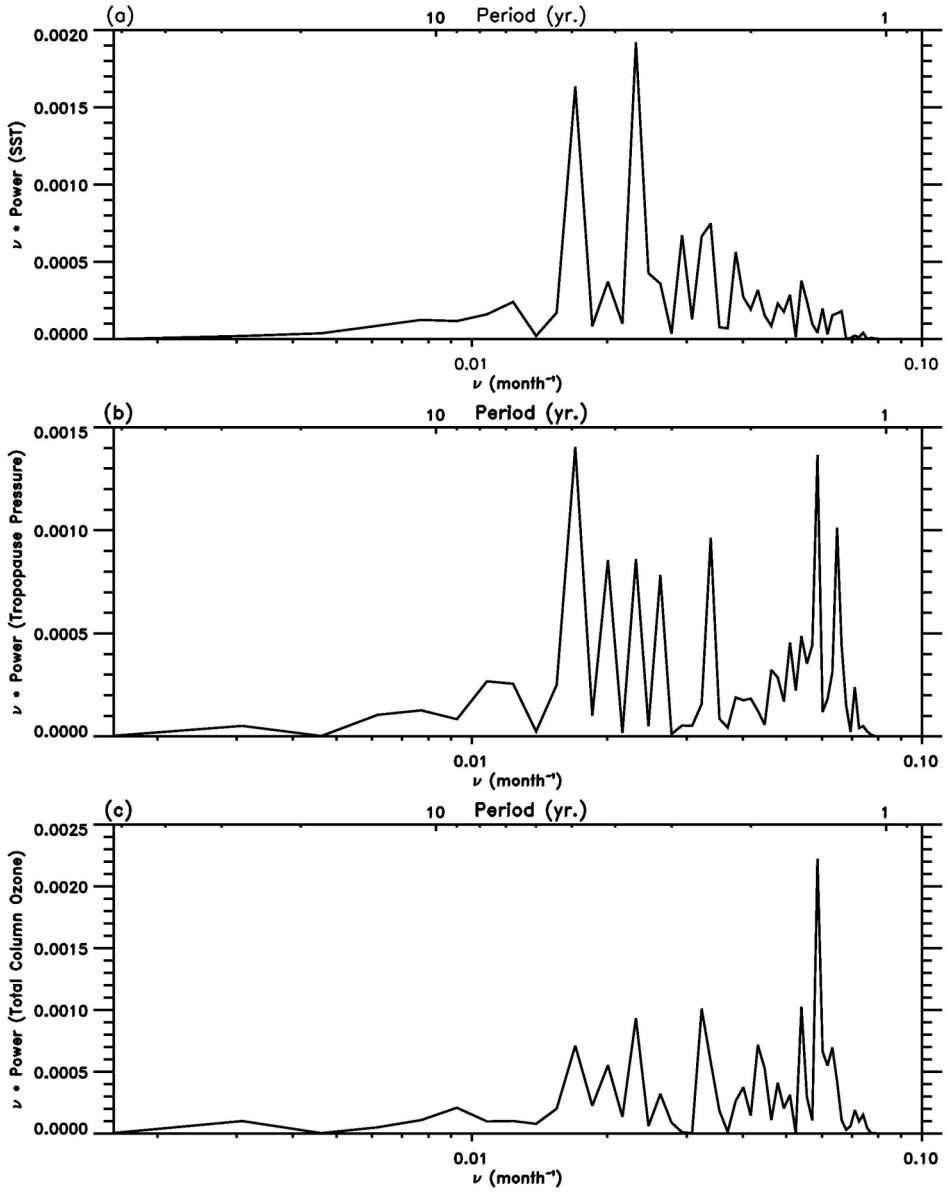

Figure 5.2. Power spectra of PC1 for first modes of GEOS CCM (a) SST, (b) P_T, and (c) Ω_S.

Figure 5.3 shows the spatial patterns of the first mode of the PCA analysis for GEOS CCM SST, P_T, and Ω_S, which describe their ENSO-related variability. For SST, the spatial pattern (Fig. 5.3a) is similar to the first mode of ENSO-related variability

described in Trenberth *et al.* (2002, see their Fig. 11), which corresponds to the SST anomalies in the Niño-3.4 region (covering 5°N–5°S, 120°W–170°W). There are warm SST anomalies in the central and western Pacific and a cold tongue in the eastern Pacific in the first mode of GEOS CCM SST. Negative amplitudes of this mode correspond to the El Niño events. During El Niño periods, the convection will move eastward to the central Pacific and impact the longitudinal structure of the tropopause (e.g., Gage and Reid, 1987; Gettelman *et al.*, 2001; Kiladis *et al.*, 2001). The spatial pattern of the first mode of P_T (Fig. 5.3b) is consistent with this behavior.

For the negative amplitudes of this mode, corresponding to El Niño events, there are large negative tropopause pressure anomalies (higher tropopause height) in the central and eastern Pacific and weak positive tropopause pressure anomalies (lower tropopause heights) in the equatorial western Pacific. Note that the tropopause pressure anomalies are relatively small over the equatorial regions. On the other hand, large tropopause pressure anomalies are found over the subtropics, which is the Rossby wave response of the equatorial ENSO convection anomaly (Trenberth *et al.*, 1998). In the positive amplitude of this mode, that is, during La Niña events, there are weak negative tropopause pressure anomalies (higher tropopause heights) in the equatorial western Pacific and large positive tropopause pressure anomalies (lower tropopause heights) in the central and eastern Pacific.

The present results are in general agreement with previous studies on the tropopause pressure and height variability associated with ENSO based on reanalysis data

(Kiladis *et al.*, 2001; Gettelman *et al.*, 2001). This indicates that the vertical movement of the tropopause associated with the ENSO is reasonably captured by the GEOS CCM.

One important aspect of the spatial pattern of the P_T anomaly is that it has the same sign everywhere except for a confined region centered over the equator to the north of Indonesia (Fig. 5.3b). Contrasting with the existence of positive and negative anomalies in the SST pattern, this means that almost the entire tropical tropopause is displaced upward (to lower pressure) in El Niño events, with a discernable signal in the zonal mean.

A similar result holds for the Ω_S pattern (Fig. 5.3c), in that substantial zonal anomalies are superimposed on a monotonic signal, which implies the forcing of the Brewer-Dobson circulation (Garcia-Herrera *et al.*, 2006) in addition to the forcing by tropical convection during El Niño events. Note that the ENSO signal dominates the variability in Ω because irradiance changes associated with the solar cycle were not included in the simulation and because this version of GEOS CCM does not simulate the QBO.

The pattern is very similar to the ENSO spatial pattern in the TOMS total column ozone data found by Camp *et al.* (2003, see their Fig. 5), although there are some differences in the Southern Hemisphere. The differences in the total column ozone in the Southern Hemisphere might arise because the model has an unrealistic representation of the Antarctic polar vortex, with too much interannual variability compared to observations (Pawson *et al.*, 2008).

The fourth mode of TOMS total column ozone obtained by Camp *et al.* (2003) is not entirely explained by the ENSO signal. There are other weak signals (*e.g.*, decadal signal) present in the fourth mode of TOMS ozone (Camp *et al.*, 2003), while there is no decadal signal in the results from model ozone. This might explain some discrepancies between model and observations. The spatial pattern of the ENSO signal in the model total column ozone is also consistent with the second mode (mature stages of the El Niño) for the total column ozone from Kayano (1997, see her Fig. 1). The value is relatively low in the western Pacific and relatively high in the eastern Pacific.

A broadly consistent picture arises from the leading anomalies, with (in El Niño events) an eastward migration of warm SST anomalies that enhance convection over the eastern Pacific where the tropopause rises and Ω_S decreases. This decrease in total column ozone is consistent with the changes of the tropopause. It is also consistent with a faster vertical flow through the ozone source region in the tropical stratosphere, which tends to reduce the total column ozone.

During El Niño, vertical propagation of Rossby wave and divergence of Eliassen-Palm flux are enhanced, accelerating the Brewer-Dobson circulation (Garcia-Herrera *et al.*, 2006). Thus, the vertical flow in the tropical stratosphere is enhanced. It leads to a decrease in total column ozone in the tropical region and an increase of total column ozone in the middle to high latitudes.

Since there is strong correspondence between total column ozone and tropopause pressure, I regress the first mode of the total column ozone on the first mode of the

tropopause pressure. The mean value for the first mode of the total column ozone in the Niño-3.4 region (5°N–5°S, 120°W––170°W) is plotted against the mean value for the first mode of the tropopause pressure in Fig. 5.4a. The Niño-3.4 region is chosen for its proximity to the Pacific warm pool and main centers of convection (Trenberth, 1997).

When the Niño-3.4 region SST anomaly is larger than 10.48°C, it corresponds to an El Niño event. The time series of total column ozone and tropopause pressure averaged in the Niño-3.4 region correlate well. The correlation coefficient is 0.82 and it is significant at the 0.1% level. The scatterplot for the two time series is shown in Fig. 5.4b. The regression coefficient between the total column ozone and tropopause pressure is 0.71 Dobson units (DU) hPa^{-1}. Assuming that the tropopause height is 10.5 km and scale height is 7 km, the regression coefficient translates to 215.5 $DUkm^{-1}$, which is consistent with the previous results that range from 210 to 225 $DUkm^{-1}$ (Meetham, 1937; Reed, 1950; Hoinka *et al.*, 1996; Steinbrecht *et al.*, 1998).

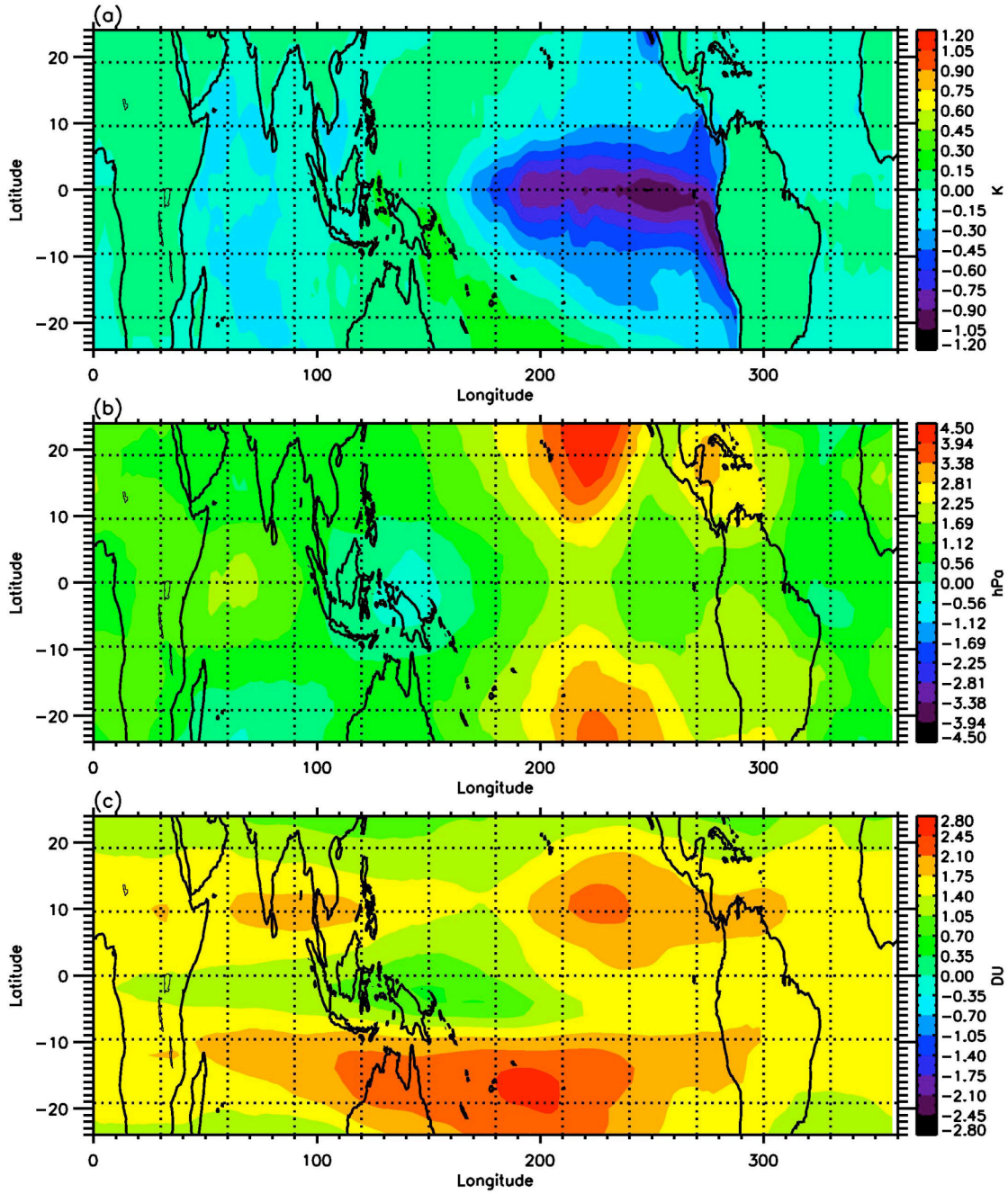

Figure 5.3. (a) Spatial pattern of first mode for GEOS CCM SST in the tropics (K). The first mode explains 46.9% of the total variance. (b) Spatial pattern of first mode for GEOS CCM P_T in the tropics (hPa). The first mode explains 33.9% of the total variance. (c) Spatial pattern of first mode for GEOS CCM Ω_S in the tropics (DU). The first mode explains 63.8% of the total variance.

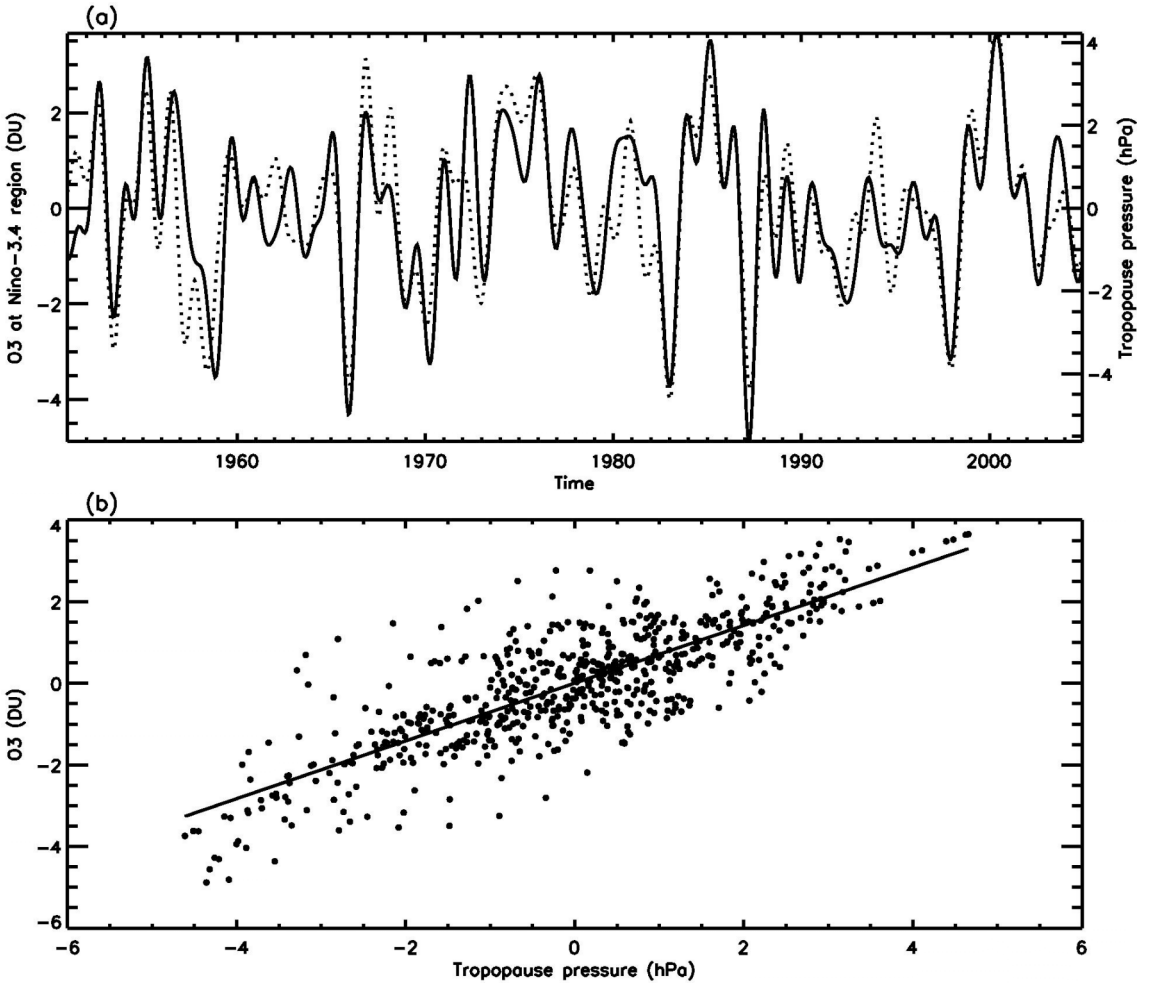

Figure 5.4. (a) First mode of GEOS CCM Ω_S averaged over the Niño-3.4 region (solid line) and first mode of GEOS CCM P_T averaged at the Niño-3.4 region (dotted line). Correlation coefficient between the two time series is 0.82 (0.1% significance level). (b) Scatter plot for GEOS CCM Ω_S and P_T. Both data averaged over the Niño-3.4 region. The solid line is the linear fit of the data.

5.5 The 3.5-yr Ozone Signal

As mentioned above, because of the vertical propagation of Rossby wave and divergence of the Eliassen-Palm flux, ENSO influences the total column ozone not only in the tropical region, but also in the middle and high latitudes. Total column ozone data at 21 stations are used to investigate an interesting interannual variability with a period of around 3.5 years. These stations are chosen for their relatively long time series (more than 20 yr). Spectral power analysis is applied to the deseasonalized and detrended total column ozone at all stations. Of the 21 stations, only eight display a significant 3.5-yr signal. The other stations have signals at 4–5 or 2–3 years. There is also no preference regarding the locations for stations with the 3.5-yr signal in the total column ozone.

The eight stations with a significant 3.5-year signal are Potsdam, Belsk, Hradec, Hohenpeissenberg, Arosa, Toronto, Sapporo, and Nashville. The geographical locations and record lengths of the eight stations are listed in Table 5.2. The power spectra and statistical significances of the peaks for the eight stations are shown in Fig. 5.5. Dotted lines are the red noise spectra. Dashed-dotted lines and dashed lines show 10% and 5% significance levels, respectively. In Fig. 5.5a, there are about five significant spectral peaks (10% significance level) in the low-frequency regions: the residual annual cycle, QBO-annual beat, QBO, 3.5-yr signal, and a decadal oscillation. Since the mechanisms for the QBO-annual beat, QBO, and the decadal oscillation are well known (Tung and Yang, 1994a, b; Jiang *et al.*, 2005; Baldwin *et al.*, 2001; Soukharev and Hood, 2006), I only focus on the 3.5-year signal in this paper.

Among the eight stations, there are significant peaks in the range of 3–4 years. The power spectra of Potsdam (Fig. 5.5a), Hohenpeissenberg (Fig. 5.5d), and Sapporo (Fig. 5.5g) lie within the 5%–10% range of significance. The significance of the 3.5-yr signals in the other five stations—Belsk (Fig. 5.5b), Hradec (Fig. 5.5c), Arosa (Fig. 5.5e), Toronto (Fig. 5.5f), and Nashville (Fig. 5.5h)—are within the 5% level. To verify the mechanism for the 3.5-yr cycle and explain the results presented above, I investigated the total column ozone signal in the GEOS CCM. Spectral analysis of the simulated total column ozone (Fig. 5.6) reveals statistically significant 3.5-yr signals at the eight stations.

TABLE 5.2. Geographical locations and record lengths of Ω_S time series observed at different stations

Station	Latitude	Longitude	Time series
Potsdam	52.36	13.08	1964–2003
Belsk	51.84	20.79	1963–2003
Hradec	50.18	15.83	1961–2005
Hohenpeissenberg	47.80	11.02	1967–2005
Arosa	46.70	9.68	1926–2005
Toronto	43.78	-79.47	1960–2003
Sapporo	43.05	141.33	1958–2005
Nashville	36.25	-86.57	1962–2004

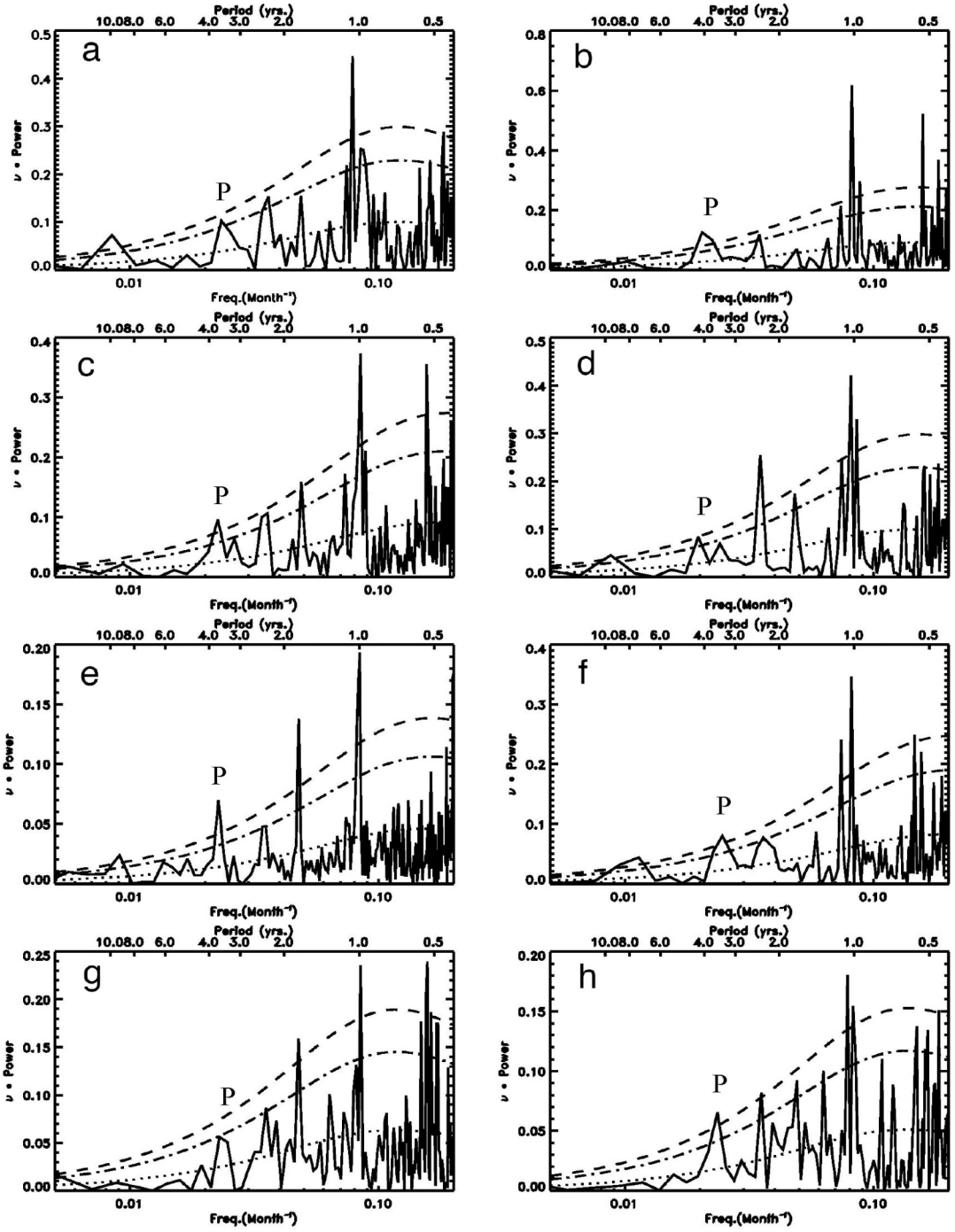

Figure 5.5. Power spectra of deseasonalized and detrended Ω_S observed at different stations: (a) Potsdam, (b) Belsk, (c) Hradec, (d) Hohenpeissenberg, (e) Arosa, (f) Toronto, (g) Sapporo, and (h) Nashville. Dotted lines are the mean red noise spectra. Dashed-dotted lines and dashed lines are 10% and 5% significance levels, respectively; P denotes the 3.5-yr signal.

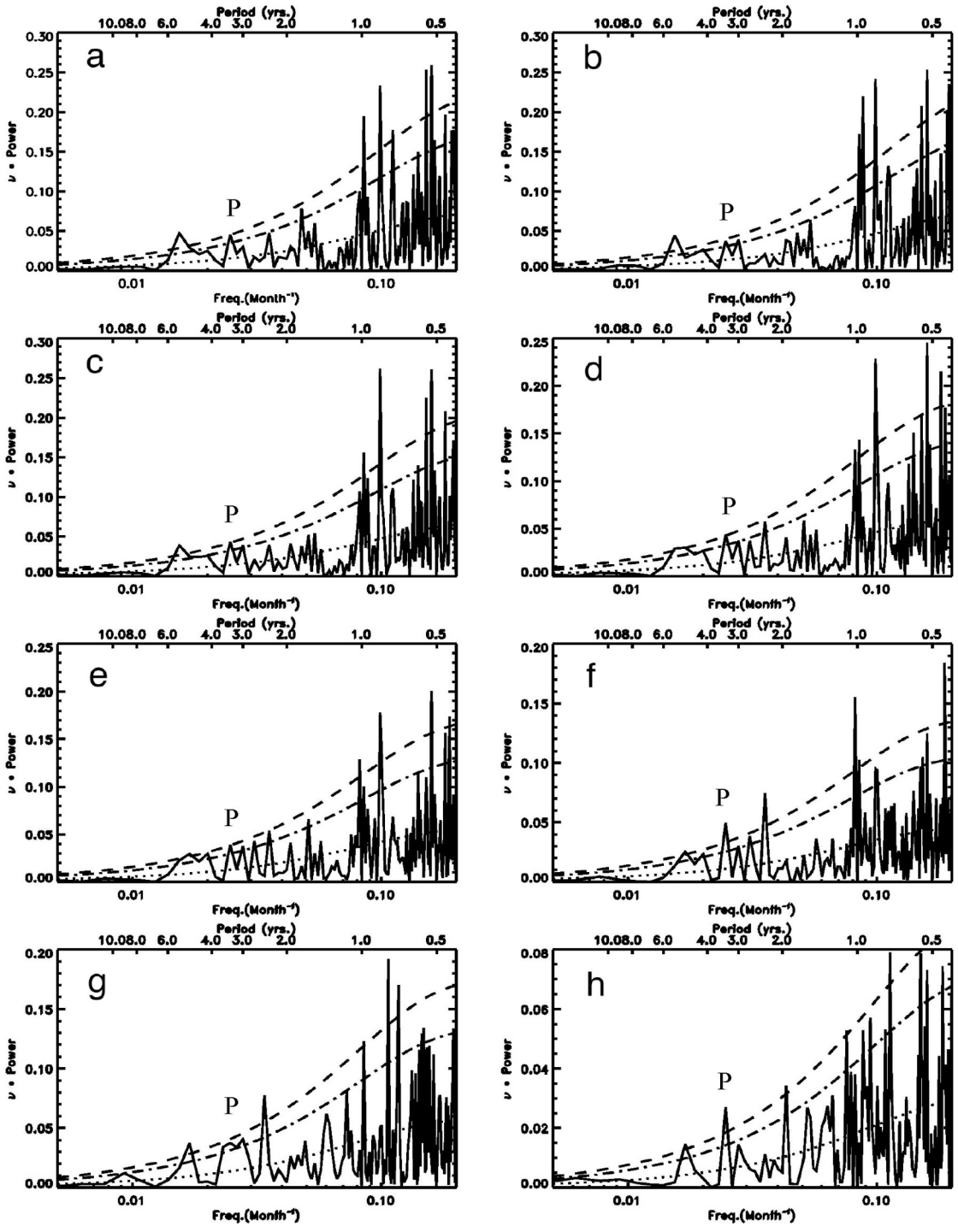

Figure 5.6. Power spectra of deseasonalized and detrended GEOS CCM Ω_S; data sample locations as for Fig. 5. Dotted lines are the mean red noise spectra. Dashed-dotted lines and dashed lines are 10% and 5% significance levels, respectively; P denotes the 3.5-yr signal.

The significance levels are within 5%–10% for the total column ozone at Potsdam, Belsk, Hradec, Hohenpeissenberg, Arosa, and Sapporo (Figs. 5.6 a–e, g), while at Toronto and Nashville (Figs. 5.6 f, h), the significance levels are better than 5%. Because the GEOS CCM simulation is forced by observed SST and sea ice distributions, its atmosphere does represent variability related to these forcings at the boundary, including ENSO events. The absence of both the QBO and solar cycle in the model means that total column ozone variations related to these phenomena are not captured. Since the 3.5-yr signal isolated in total column ozone observations is captured at a significant level in the GEOS CCM, this suggests that this signal originates from the ENSO signal in SST forcing rather than from other forced variations in stratospheric ozone, although on the basis of this analysis we cannot preclude the possibility that internal (unforced) dynamics cause this signal.

5.6 Conclusions

In this chapter, I have studied the ENSO signal in the tropical total column ozone and tropical tropopause pressure in the GEOS CCM from January 1951 to December 2004. The first modes in the model tropical total column ozone and tropopause pressure capture 63.8% and 33.9% of the total variances, respectively. The PC1 for the first modes in the model total column ozone and tropopause pressure correlate well with the low-pass filtered SOI index and leading PC time series for the SST. The spatial pattern of the first mode for the model total column ozone is similar to the ENSO signal in the TOMS total column ozone, although there are some discrepancies for the total column ozone in the Southern Hemisphere. The regression coefficient between the model total column ozone and the model tropopause pressure is consistent with that found from observations. In the

middle latitudes, I applied spectral analysis to the observed monthly mean total column ozone data and find the 3.5-yr signal, within the 10% significance level, at eight stations. The 3.5-yr signal is also found in the GEOS CCM model total column ozone. Since GEOS CCM does have a realistic ENSO signal and does not have a QBO or a solar cycle, the results suggest that the 3.5-yr signal in total column ozone is related to the ENSO signal. The linkage between 3.5-yr ozone signal and surface ENSO needs to be investigated in more detail in the future, for example, by using controlled model experiments in which the ENSO forcing is removed.

5.7 Acknowledgments

I thank Bernhard Rappenglueck, Barry Lefer, and Mimi Gerstell for useful inputs and helpful comments. I thank the World Ozone and Ultraviolet Radiation Data Centre for providing the ozone observation data.

Chapter 6

Conclusions

This work used satellite retrievals, observation data, and chemistry transport models to study the variability of the tracer gases Carbon Dioxide and Ozone.

First, the influence of Tropospheric Biennial Oscillation (TBO) on the mid-tropospheric CO_2 was discovered by utilizing AIRS mid-tropospheric CO_2 retrievals and the MOZART-2 chemistry-transport model. The relationship between the TBO and variations of mid-tropospheric CO_2 concentrations over the Indo-Pacific region was established. Time series of AIRS mid-tropospheric CO_2 correlate well with the TBO index, showing that during strong monsoon years, there is more CO_2 in the mid-troposphere over Indonesia due to the strong Western Walker Cell, and a lower CO_2 concentration in weak monsoon years due to weak convection. The comparison of the time series of monsoon index and detrended deseasonalized CO_2 concentation suggested the strength of the circulation influences CO_2 concentration in the mid-troposphere. MOZART-2 mid-tropospheric CO_2 results to be consistent with the results from the observation, although the signal simulated in the model is smaller than that from AIRS CO_2. Due to the weakness in the model meteorological fields and CO_2 boundary conditions, TBO might not be fully represented in the model. The correct identification of this natural variability of CO_2 is important for inferring the sources, sinks, and transport

of CO_2. In addition, as the quality and quantity of satellite CO_2 data improve (*Boesch et al.*, 2011), modeling the variations in the mid-tropospheric CO_2 as a response to monsoon offers a unique opportunity to diagnose deficiencies in chemistry-transport models.

Second, I investigated a major Stratospheric Sudden Warming (SSW) event that occurred in March 2005. The SSW lasted for about eleven days (Days 72 to 82). Before the SSW, the wind was westerly and EP-flux divergence was negative. The CO_2 concentration was low in the polar region especially in the polar vortex center. During the SSW, the polar vortex was weak and destroyed, the westerly wind switched into the easterly wind. The mean temperature increased by 2.5K. The EP-flux divergence was positive after the SSW, the easterly wind decreased, and the westerly zonal wind increased. SSW also has influence on the mid-tropospheric CO_2 concentrations. After the SSW, the mean value of CO_2 concentrations in the polar region increased by 2.5 ppmv, which was a result of shrinking of the polar vortex area and reduced mixing between the stratosphere and troposphere.

Next, I used the MOZART-2 model to investigate the interannual variability of CO_2 in the (NH) tropical region. The detrended mid-tropospheric CO_2 difference between the central and western Pacific Oceans correlates well with the inverted and detrended SOI. There is more model mid-tropospheric CO_2 in the central Pacific Ocean and less model mid-tropospheric CO_2 in the western Pacific Ocean during the El Niño events. In La Niña years, the CO_2 concentrations in the central Pacific Ocean are lower than those in the western Pacific Ocean. The model results were consistent with the observations,

although the amplitude and spatial pattern in the model mid-tropospheric CO_2 was a little different compared with that in the AIRS mid-tropospheric CO_2. These results will be very helpful for modelers to better simulate ENSO signals in the middle troposphere and better constrain vertical transport in the chemistry-transport models.

Finally, I studied the ENSO signal in the tropical total column ozone and tropical tropopause pressure in the GEOS CCM from January 1951 to December 2004. The first modes in the model tropical total column ozone and tropopause pressure capture 63.8% and 33.9% of the total variances, respectively. The PC1 for the first modes in the model total column ozone and tropopause pressure correlate well with the low-pass filtered SOI index and leading PC time series for the SST. The spatial pattern of the first mode for the model total column ozone is similar to the ENSO signal in the TOMS total column ozone, although there are some discrepancies for the total column ozone in the Southern Hemisphere. The regression coefficient between the model total column ozone and the model tropopause pressure is consistent with that found from observations. In the middle latitudes, I applied spectral analysis to the observed monthly mean total column ozone data and found the 3.5-yr signal, within the 10% significance level, at eight stations. The 3.5-yr signal is also found in the GEOS CCM model total column ozone. Since GEOS CCM does have a realistic ENSO signal and does not have a QBO or a solar cycle, the results suggest that the 3.5-yr signal in total column ozone is related to the ENSO signal.

References

Andrews, D. G., J. R. Holton, and C. B. Leovy, 1987: *Middle Atmosphere Dynamics,* pp. 123-133.

Aumann, H. H. *et al.*, 2003: AIRS/AMSU/HSB on the Aqua mission: design, science objectives, data products, and processing systems. IEEE Trans. *Geosci. Remote Sens.,* **41,** 253.

Bacastow, R., 1976: Modulation of atmospheric carbon dioxide by the Southern Oscillation. *Nature,* **261,** 116-118, doi:10.1038/261116a0.

Bacastow, R., J. Adams, C. Keeling, D. Moss, T. Whorf, and C. Wong, 1980: Atmospheric carbon dioxide, the Southern Oscillation, and the weak 1975 El Niño. *Science,* **210**, 66-68, doi: 10.1126/science.210.4465.66.

Bacastow, R. B., C. D. Keeling, and T. P. Whorf, 1985: Seasonal amplitude increase in atmospheric CO_2 concentration at Mauna Loa, Hawaii, 1959-1982. *Journal of Geophysical Research*, **90,** 10529-10540.

Baldwin M. P., *et al.*, 2001: The quasi-biennial oscillation. *Rev. Geophys.,* **39,** 179-229.

Baldwin, M. P., and T. J. Dunkerton, 2001: Stratospheric harbingers of anomalous weather regime. *Science*, **294,** 581-584.

Boesch, H., D. Baker, B. Connor, D. Crisp, and C. Miller, 2011: Global characterization of CO_2 column retrievals from shortwave-infrared satellite observations of the Orbiting Carbon Observatory-2 Mission. *Remote Sensing*, **3,** 270-304.

Bojkov, R. D., 1987: The 1983 and 1985 anomalies in ozone distribution in perspective. *Mon. Wea. Rev.,* **115**, 2187-2201.

Buermann, W., B. Lintner, C. Koven, A. Angert, J. E. Pinzon, C. J. Tucker, and I. Fung, 2007: The changing carbon cycle at the Mauna Loa observatory. *Proc. Nat. Acad. Sci.*, **104**, 4249-4254.

Cagnazzo, C. *et al.,* 2009: Northern winter stratospheric temperature and ozone responses to ENSO inferred from an ensemble of Chemistry Climate Models. *Atmospheric Chemistry and Physics*, **9**, 8935-8948.

Camp, C. D., M. S. Roulston, and Y. L. Yung, 2003: Temporal and spatial patterns of the interannual variability of total ozone in the tropics. *J. Geophys. Res,* **108**, D4643, doi:10.1029/2001JD001504.

Chahine, M., C. Barnet, E. T. Olsen, L. Chen, and E. Maddy, 2005: On the determination of atmospheric minor gases by the method of vanishing partial derivatives with application to CO_2. *Geophys. Res. Lett.*, **32**, doi:10.1029/2005GL024165.

Chahine, M., L. Chen, P. Dimotakis, X. Jiang, Q. Li, E. T. Olsen, T. Pagano, J. Randerson, and Y. L. Yung, 2008: Satellite remote sounding of mid-tropospheric CO_2. *Geophys. Res. Lett.*, **35**, doi:10.1029/2008GL035022.

Chandra, S., J. R. Ziemke, W. Min, and W. G. Read, 1998: Effects of 1997-1998 El Niño on tropospheric ozone and water vapor. *Geophys. Res. Lett.,* **25***,* 3867-3870.

Chang, C. P. and T. Li, 2000: A theory for the tropical tropospheric biennial oscillation. *J. Atmos. Sci.,* **57,** 2209-2224.

Chang, C. P., and T. Li, 2001: Nonlinear interactions between the TBO and ENSO, east Asian and western Pacific meteorology and climate. *Book Series on East Asian Meteorology, World Scientific Publishing Company,* Singapore, **1,** 25-38.

Cleveland, M. S., A. E. Freeny, and T. E. Graedel, 1983: The seasonal component of atmospheric CO_2: Information from new approaches to the decomposition of seasonal time series. *Journal of Geophysical Research*, **88**, 10934-10946.

Curry, J. A., and J. L. Schramm, 1994: Sea ice-albedo climate feedback mechanism. *J. of Climate,* **8,** 240-247.

Dargaville, R. J., R. M. Law, and F. Pribac, 2000: Implications of interannual variability in atmospheric circulation on modeled CO_2 concentrations and source estimates. *Glob. Biogeochem. Cyc.*, **14**, 931-943.

Dettinger, M. D., and M. Ghil, 1998: Seasonal and interannual variations of atmospheric CO_2 and climate. *Tellus, ser. B*, **50**, 1-24.

Dickinson, R. E., and R. J. Cicerone, 1986: Future global warming from atmospheric trace gases. *Nature,* **319(6049),** 109-115, doi:10.1038/319109a0.2 doi:10.1029/96JD03131.

Dobson, G. M. B., 1931: A photoelectric spectrophotometer for measuring the amount of atmospheric ozone. *Proceeding of the Physical Society,* **43,** 324- 339.

Douglass, A. R., M. R. Schoeberl, and R. B. Rood, 2003: Evaluation of transport in the lower tropical stratosphere in a global chemistry and transport model. *Journal of Geophysical Research,* **108**, D4259, doi:10.1029/2002JD002696.

Duncan, B. N. *et al.*, 2003: Interannual and seasonal variability of biomass burning emissions constrained by satellite observations. *Journal of Geophysical Research*, **108,** doi:10.1029/2002JD002378.

Dunteman, G. H., 1989: *Principal Components Ahanlysis*, International Education and Professional Publisher, 98pp.

Eliassen, A. and E. Palm, 1961: On the transfer of energy in stationary mountain waves. *Geofys. Publ.,* **22,** 1-23.

Enting, I. G., 1987: The interannual variation in the seasonal cycle of carbon dioxide concentration at Mauna Loa. *Journal of Geophysical Research*, **92**, 5497-5504, 1987.

Eyring, V., and Coauthors, 2006: Assessment of temperature, trace species, and ozone in chemistry-climate model simulations of the recent past. *Journal of Geophysical Research,* **111,** D22308, doi:10.1029/2006JD007327.

Fabry, C., and H. Buisson, 1913: L'absorption de l'ultraviolet par l'ozone et la limite du spectre solaire. *J. Phys. Rad. , Serie 5,* **3,** 196- 206.

Feely, R. A., and Coauthors, 1987: Distribution of chemical tracers in the eastern equatorial Pacific during and after the 1982/1983 ENSO event. *Journal of Geophysical Research*, **92**, 6545-6558.

Free, M., and D. J. Seidel, 2009: Observed El Niño-Southern Oscillation temperature signal in the stratosphere. *Journal of Geophysical Research,* **114,** D23108, doi:10.1029/2009JD012420.

Gage, K.S., and G. C. Reid, 1987: Longitudinal variations in tropical tropopause properties in relation to tropical convection and El Niño-Southern Oscillation. *Journal of Geophysical Research,* **92,** 14,197-14,203.

Garcia-Herrera, R., N. Calvo, R. R. Garcia, and M. A. Giorgetta, 2006: Propagation of ENSO temperature signals into the middle atmosphere: A comparison of two general circulation models and ERA-40 reanalysis data. *Journal of Geophysical Research*, **111**, D06101, doi:10.1029/2005JD006061.

Gettelman, A., W. J. Randel, S. Massie, F. Wu, W. G. Read, and J. M. Russell III, 2001: El Niño as a natural experiment for studying the tropical tropopause region. *J. Climate,* **14,** 3375-3392.

Gilman, D. L., F. J. Fuglister, and J. M. Mitchell, 1963: On the power spectrum of "red noise". *J. Atmos. Sci.,* **20,** 182-184.

Hardiman, S. C. *et al.*, 2011: Improved predictability of the troposphere using stratospheric final warmings. *Journal of Geophysical Research,* **116,** D18113, doi:10.1029/2011JD015914

Hasebe, F., 1993: Dynamical response of the tropical total ozone to sea surface temperature changes. *J. Atmos. Sci.,* **50,** 345-356.

Hoinka, K. P., H. Claude, and U. Kohler, 1996: On the correlation between tropopause pressure and ozone above central Europe. *Geophys. Res. Lett.,* **23,** 1753-1756.

Holland, M. M. and C. M. Bitz, 2003: Polar amplification of climate change in coupled modles. *Climate Dynamics,* **21,** 221-232, DOI 10.1007/s00382-003-0332-6.

Hood, L. L., B. E. Soukharev, and J. P. McCormack, 2010: Decadal variability of the tropical stratosphere: secondary influence of the El Nino-Southern Oscillation. *Journal of Geophysical Research*, **115**, D11113, doi:10.1029/2009JD012291.

Horinouchi, T., S. Pawson, K. Shibata, U. Langematz, E. Manzini, M. A. Giorgetta, F. Sassi, R. J. Wilson, K. P. Hamilton, J. de Grandpré, A. A. Scaife, 2003: Tropical cumulus convection and upward propagating waves in middle atmospheric GCMs. *J. Atmos. Sci.,* **60,** 2765-2782.

Horowitz, L. W., S. Walters, D. L. Mauzerall, L. K. Emmons, P. J. Rasch, C. Granier, X. Tie, J. F. Lamarque, M. G. Schultz, and G. P. Brasseur, 2003: A global simulation of tropospheric ozone and related tracers: Description and evaluation of MOZART, version 2. *Journal of Geophysical Research,* **108,** 4784, doi:10.1029/2002JD002853.

Huffman, G. J. *et al.*, 2007: The TRMM multi-satellite precipitation analysis: Quasi-Global, Multi-Year, Combined-Sensor precipitation estimates at fine scale. *J. Hydrometeor.*, **8,** 33-55.

Huffman, G. J., R. F. Adler, D. T. Bolvin, and G. J. Gu, 2009: Improving the global precipitation record: GPCP version 2.1. *Geophys. Res. Lett.*, **36,** doi:10.1029/2009GL040000.

Intergovernmental Panel on Climate Change (IPCC), 2001: Climate Change 2000—Third Assessment Report. *Cambridge University Press,* Cambridge .

IPCC, 2007: Climate Change 2007: The Physical Science Basis. Contribution of Working Group I to the Fourth Assessment Report of the Intergovernmental Panel on

Climate Change. *Cambridge University Press, Cambridge, United Kingdom and New York, NY, USA.*

Jiang, X., D. B. A. Jones, R. Shia, D. E. Waliser, and Y. L. Yung, 2005: Spatial patterns and mechanisms of the Quasi-Biennial Oscillation-Annual Beat of ozone. *Journal of Geophysical Research,* **110,** D23308, doi:10.1029/2005JD006055.

Jiang, X., Q. Li, M. Liang, R. L. Shia, M. T. Chahine, E. T. Olsen, L. L. Chen, and Y. L. Yung, 2008: Simulation of upper troposphere CO_2 from chemistry and transport models. *Global Biogeochem. Cycles*, **22**, doi:10.1029/2007GB003049.

Jiang, X., S. Pawson, C. D. Camp, E. Nielsen, R. Shia, T. Liao, K. Jeev, V. Limpasuvan, and Y. L. Yung, 2008a: Interannual variability and trends in extratropical ozone. Part I: Northern hemisphere. *J. Atmos. Sci.,* **65,** 3013-3029.

Jiang, X., Q. Li, M. Liang, R. L. Shia, M. T. Chahine, E. T. Olsen, L. L. Chen, and Y. L. Yung, 2008b: Simulation of upper troposphere CO_2 from chemistry and transport models. *Global Biogeochem. Cycles*, **22,** doi:10.1029/2007GB003049.

Jiang, X., M. T. Chahine, E. T. Olsen, L. Chen, and Y. L. Yung, 2010: Interannual variability of mid-tropospheric CO_2 from Atmospheric Infrared Sounder. *Geophysical Research Letters*, 2010GL042823.

Jiang, X., J. Wang, E. T. Olsen, M. Liang, T. Pagano, L. L. Chen, S. Licata, and Y. Yung, 2012: Influence of ENSO on mid-tropospheric CO_2 from Atmospheric Infrared Sounder. *Submitted to JAS.*

Jones, C. D., M. Collins, P. M. Cox, and S. A. Spall, 2001: The carbon cycle response to ENSO: A coupled climate-carbon cycle model study. *Journal of Climate,* **14,**

4113-4129, doi: 10. 1175/ 1520- 0442 (2001) 014<4113: TCCRTE>2.0.CO;2.

Kayano, M. T., 1997: Principal modes of the total ozone on the Southern Oscillation timescale and related temperature variations. *Journal of Geophysical Research,* **102,** 25797-25806.

Keeling, C. D., and R. Revelle, 1985: Effects of ENSO on the atmospheric content of CO_2. *Meteroritics*, **20**, 437-450.

Keeling, C. D., T. P. Whorf, M. Wahlen, and J. Vanderplicht, 1995: Interannual extremes in the rate of rise of atmospheric carbon dioxide since 1980. *Nature*, **375**, 666-670.

Keeling, C. D., J. F. S. Chin, and T. P. Whorf, 1996: Increased activity of northern hemispheric vegetation inferred from atmospheric CO_2 measurements. *Nature*, **382**, 146-149.

Keppel-Aleks, G., P. O. Wennberg, and T. Schneider, 2011: Sources of variations in total column carbon dioxide. *Atmos. Chem. Phys*., **11,** 3581-3593.

Kiladis, G. N., Straub K. H., Reid G. C., and Gage K. S., 2001: Aspects of interannual and intraseasonal variability of the tropopause and lower stratosphere. *Quart. J. Roy. Meteor. Soc.*, **127,** 1961-1983.

Kita, K., M. Fujiwara, and S. Kawakami, 2000: Total ozone increase associated with forest fires over the Indonesian region and its relation to the El Nino-Southern oscillation. *Atmos. Envir.,* **34,** 2681-2690.

Lau, K. M., and S. Yang, 1996: The Asian monsoon and predictability of the tropical ocean-atmosphere system. *Q. J. Roy. Meteorol. Soc.,* **122,** 945-957.

Li, K. F., B. Tian, D. E. Waliser, and Yuk L. Yung, 2010: Tropical mid-tropospheric CO_2 variability driven by the Madden-Julian Oscillation, *Proceedings of the National Academy of Sciences of the United States of America,* **107,** 19171-19175.

Li, Q., J. H. Jiang, D. L. Wu, W. G. Read, N. J. Livesey, J. W. Waters, Y. Zhang, B. Wang, M. J. Filipiak, C. P. Davis, S. Turquety, S. Wu, R. J. Park, R. M. Yantosca, and D. J. Jacob, 2005: Convective outflow of South Asian pollution: A global CTM simulation compared with EOS MLS observations. *Geophys. Res. Lett.*, **32,** doi:10.1029/2005GL022762.

Limpasuvan, V. and D. L. Hartmann, 1999: Eddies and the annular modes of climate variability, *Geophysical Research Letters*, **26**, 3133-3136.

Limpasuvan, V., D. W. J. Thompson, and D. L. Hartmann, 2004: The life cycle of the northern hemisphere sudden stratospheric warmings. *J. Climate,* **17**, 2584-2596.

Marland, G., T. A. Boden, and R. J. Andres, 2007: Global, regional, and national CO_2 emissions. *In Trends: A Compendium of Data on Global Change. Carbon Dioxide Information Analysis Center*. Oak Ridge National Laboratory, U.S. Department of Energy, Oak Ridge, Tenn.

Meehl, G. A., 1997: The South Asian monsoon and the tropospheric biennial oscillation (TBO). *J. Climate,* **10,** 1921-1943.

Meehl, G. A., and J. M. Arblaster, 2002: The Tropospheric Biennial Oscillation and Asian-Australian monsoon rainfall. *J. Climate,* **15,** 722-744.

Meetham, A. R., 1937: The correlation of the amount of ozone with other characteristics of the atmosphere. *Quart. J. Roy. Meteor. Soc.,* **63,** 289-307.

Mooley, D. A., and B. Parthasarathy, 1984: Fluctuations in All-India summer monsoon rainfall during 1871-1978. *Climatic Change,* **6,** 287-301.

Nevison, C. D., *et al*., 2008: Contribution of ocean, fossil fuel, land biosphere, and biomass burning carbon fluxes to seasonal and interannual variability in 26 atmospheric CO_2. *Journal of Geophysical Research*, **113,** 27 doi:10.1029/2007JG000408.28

Olsen *et al.*, 2011: Validation of the AIRS mid-tropospheric CO_2 retrievals by the Vanishing Partial Derivative Method, *Submitted to JGR*.

Pawson, S., R. S. Stolarski, A. R. Douglass, P. A. Newman, J. E. Nielsen, S. M. Frith, and M. L. Gupta, 2008: Goddard Earth Observing System chemistry-climate model simulations of stratospheric ozone-temperature coupling between 1950 and 2005. *Journal of Geophysical Research,* **113,** D12103, doi:10.1029/2007JD009511.

Pearman, G. I., and P. Hyson, 1980: Activities of the global biosphere as reflected in atmospheric CO_2 records. *Journal of Geophysical Research*, **85,** 4468-4474.

Pearman, G. I., and P. Hyson, 1981: The annual variation of atmospheric CO_2 concentration observed in the northern hemisphere. *Journal of Geophysical Research*, **86,** 9839-9843.

Preisendorfer, R. W., 1988: Principal component analysis in meteorology and oceanography. *Dev. in Atmos. Sci.,* **17,** 425 p.

Press, W., S. Teukolsky, W. Vetterling, and B. Flannery, 1992: *Numerical Recipes in Fortran 77: The Art of Scientific Computing.* Cambridge Univ. Press, New York, 933 pp.

Prinn, R. G., *et al.*, 2000: A history of chemically and radiatively important gases in air deduced from ALE/GAGE/AGAGE, *Journal of Geophysical Research,* **105,** 17,751-17,792, doi:10.1029/2000JD900141.

Räisänen, J. 2001: CO_2-induced climate change in CMIP2 experiments: Quantification of agreement and role of internal variability. *J. Climate*, **14,** 2088–2104.

Randerson, J. T. *et al.*, 1997: The contribution of terrestrial sources and sinks to trends in the seasonal cycle of atmospheric carbon dioxide. *Global Biogeochem. Cycles*, **11,** 535-560.

Rayner, N. A., D. E. Parker, E. B. Horton, C. K. Folland, L. V. Alexander, D. P. Rowell, E. C. Kent, and A. Kaplan, 2003: Global analyses of sea surface temperature, sea ice, and night marine air temperature since the late nineteenth century. *Journal of Geophysical Research,* **108**, D4407, doi:10.1029/2002JD002670.

Reed, R. J., 1950: The role of vertical motions in ozone-weather relationship. *J. Meteor.,* **7,** 263-267.

Ropelewski, C. F., M. S. Halpert, and X. Wang, 1992: Observed tropospheric biennial variability and its relationship to the Southern Oscillation. *J. Climate,* **5,** 594-614.

Schubert, S. D., and M. J. Munteanu, 1988: An analysis of tropopause pressure and total ozone correlations. *Mon. Wea. Rev.,* **116,** 569-582.

Shen, S., and K. M. Lau, 1995: Biennial oscillation associated with the East Asian monsoon and tropical sea surface temperatures. *J. Meteor. Soc. Japan,* **73,** 105-124.

Shia, R., M. Liang, C. E. Miller, and Y. L. Yung, 2006: CO_2 in the upper troposphere: Influence of stratosphere-troposphere exchange. *Geophys. Res. Lett.,* **33,** L14814, doi:10.1029/2006GL026141.

Shiotani, M., 1992: Annual, quasi-biennial, and El Niño-Southern Oscillation (ENSO) timescale variations in equatorial total ozone. *Journal of Geophysical Research,* **97,** 7625-7633.

Soukharev, B. E., and L. L. Hood, 2006: Solar cycle variation of stratospheric ozone: Multiple regression analysis of long-term satellite data sets and comparisons with models. *Journal of Geophysical Research,* **111,** D20314, doi:10.1029/2006JD007107.

Steinbrecht, W., H. Claude, U. Kohler, and K. P. Hoinka, 1998: Correlations between tropopause height and total ozone: Implications for long-term changes. *Journal of Geophysical Research,* **103,** 19183-19192.

Stolarski, R. S., A. R. Douglass, S. E. Steenrod, S. Pawson, 2006: Trends in stratospheric ozone: Lessons learned from a 3D chemical transport model. *J. Atmos. Sci.,* **63,** 1028-1041.

Sturman, A. P., N. Tapper, 1996: The weather and climate of Australia and New Zealand. Oxford, 475pp.

Takahashi, T. *et al.*, 1997: Global air-sea flux of CO_2: An estimate based on measurements of sea-air pCO_2 difference. *Proc. Natl. Acad. Sci. U. S. A.*, **94,** 8929.

Thompson, D.W.J., and J.M. Wallace, 1998: The Arctic Oscillation signature in the wintertime geopotential height and temperature fields. *Geophys. Res. Lett.*, **25**, 1297-1300.

Thompson, A. M., and R. D. Hudson, 1999: Tropical tropospheric ozone (TTO) maps from Nimbus 7 and Earth Probe TOMS by the modified-residual method: Evaluation with sondes, ENSO signals, and trends from Atlantic regional time series. *Journal of Geophysical Research,* **104,** 26961-26975.

Thompson, D. W. J., and J. M. Wallace, 2000: Annular modes in the extratropical circulation. Part I: Month-to-month variability. *J. Climate,* **13,** 1000-1016.

Tian, S. F., and T. Yasunari, 1992: Time and space structure of interannual variation in summer rainfall over China. *J. Meteor. Soc. Japan,* **70,** 585-596.

Tian, B., Y. L. Yung, D. E. Waliser, T. Tyranowski, L. Kuai, E. J. Fetzer, and F. W. Irion, 2007: Intraseasonal variations of the tropical total ozone and their connection to the Madden-Julian Oscillation. *Geophys. Res. Lett.,* **34,** L08704, doi:10.1029/2007GL029451.

Trenberth, K. E., and D. J. Shea, 1987: On the evolution of the Southern Oscillation event. *Mon. Wea. Rev.,* **115,** 3078-3096.

Trenberth, K. E., 1997: The definition of El Niño. *Bull. Amer. Met. Soc.,* **78**, 2771-2777.

Trenberth, K. E., 1998: Progress during TOGA in understanding and modeling global teleconnections associated with tropical sea surface temperatures. *Journal of Geophysical Research,* **103,** 14291-14324.

Trenberth, K. E., J. M. Caron, D. P. Stepaniak, and S. Worley, 2002: Evolution of El Niño-Southern Oscillation and global atmospheric surface temperatures. *Journal of Geophysical Research,* **107**, doi: 10.1029/2000JD000298.

Tung, K. K., and H. Yang, 1994a: Global QBO in circulation and ozone: 1. Reexamination of observational evidence. *J. Atmos. Sci.*, **51,** 2699-2707.

Tung, K. K., and H. Yang, 1994b: Global QBO in circulation and ozone: 2. A simple mechanistic model. *J. Atmos. Sci.*, **51,** 2708-2721.

Washenfelder, R. A., G. C. Toon, J.-F. Blavier, Z. Yang, N. T. Allen, P. O. Wennberg, S. A. Vay, D. M. Matross, and B. C. Daube, 2006: Carbon dioxide column abundances at the Wisconsin Tall Tower site. *Journal of Geophysical Research,* **111,** D22305, doi:10.1029/2006JD007154.

Waugh, D.W., & Rong, P.P, 2002: Interannual variability in the decay of lower stratospheric Arctic vortices. *J. Meteor. Soc. Japan*, **80,** 997-1012, 2002.

Webster, P. J., A. M. Moore, J. P. Loschnigg, and R. R. Leben, 1999: Coupled ocean-atmosphere dynamics in the Indian Ocean during 1997-98. *Nature,* **401,** 356-360.

Yang, Z., R. A. Washenfelder, G. Keppel-Aleks, N. Y. Krakauer, J. T. Randerson, P. P. Tans, C. Sweeney, and P. O. Wennberg, 2007: New constraints on Northern Hemisphere growing season net flux. *Geophys. Res. Lett.*, **34,** doi:10.1029/2007GL029742.

Yasunari, T. and R. Suppiah, 1988: Some problems on the interannual variability of Indonesian monsoon rainfall. *Tropical Rainfall Measurements,* J. S. Theon and N. Fugono, Eds., Deepak, 113-122.

Yasunari, T., 1990: Impact of Indian monsoon on the coupled atmosphere ocean system in the tropical Pacific, *Meteor. Atmos. Phys.,* **44,** 29-41.

Yasunari, T., 1991: The monsoon year—A new concept of the climate year in the Tropics. *Bull. Amer. Meteor. Soc.,* **72,** 1331-1338.

Yokota, T., Y. Yoshida, N. Eguchi, Y. Ota, T. Tanaka, H. Watanabe, and S. Maksyutov, 2009: Global concentrations of CO2 and CH4 retrieved from GOSAT: First preliminary results, *SOLA*, **5,** 160-163.

Zerefos, C. S., A. F. Bais, I. C. Ziomas, and R. D. Bojkov, 1992: On the relative importance of Quasi-Biennal Oscillation and El Niño/Southern Oscillation in the revised Dobson total ozone records. *Journal of Geophysical Research,* **97,** 10135-10144.